PCCP

An insight into the corrosion of alkali aluminoborosilicate glasses in acidic environments

Journal:	*Physical Chemistry Chemical Physics*
Manuscript ID	CP-ART-11-2019-006064.R1
Article Type:	Paper
Date Submitted by the Author:	17-Dec-2019
Complete List of Authors:	Stone-Weiss, Nicholas; Rutgers The State University of New Jersey, Department of Materials Science and Engineering Yougman, Randall; Corning Inc, Science and Technology Division Thorpe, Ryan; Rutgers The State University of New Jersey, Department of Physics and Astronomy and Laboratory for Surface Modification Smith, Nicholas; Corning Inc, Science and Technology Division Pierce, Eric; Oak Ridge National Laboratory, Environmental Sciences Division Goel, Ashutosh; Rutgers The State University of New Jersey, Department of Materials Science and Engineering

An insight into the corrosion of alkali aluminoborosilicate glasses in acidic environments

Nicholas Stone-Weiss,[1] Randall E. Youngman,[2] Ryan Thorpe,[3] Nicholas J. Smith,[2] Eric M. Pierce,[4] Ashutosh Goel[1*]

[1]Department of Materials Science and Engineering, Rutgers, The State University of New Jersey, Piscataway, NJ, 08854, United States

[2]Science and Technology Division, Corning Incorporated, Corning, NY 14831, United States

[3]Department of Physics and Astronomy and Laboratory for Surface Modification, Rutgers, The State University of New Jersey, Piscataway, NJ, 08854, United States

[4]Environmental Sciences Division, Oak Ridge National Laboratory, Oak Ridge, TN 37831, United States

[*] Email: ag1179@soe.rutgers.edu; Ph: +1-848-445-4512

Abstract

The majority of the literature on glass corrosion focuses on understanding the dissolution kinetics and mechanisms of silicate glass chemistries in the neutral–to–alkaline aqueous regime owing to its relevance in the fields of nuclear waste immobilization and biomaterials. However, understanding the corrosion of silicate-based glass chemistries over a broad composition space in the acidic pH regime is essential for glass packaging and touch screen electronic display industries. A thorough literature review on this topic reveals only a handful of studies that discuss acid corrosion of silicate glasses and their derivatives—these include only a narrow set of silicate-based glass chemistries. Although the current literature successfully explains the dissolution kinetics of glasses based upon classically understood aqueous corrosion mechanisms, more recent advancements in atomic-scale characterization techniques, have enabled a better understanding of reactions taking place directly at the pristine glass–fluid interface which has facilitated the development of a unifying model describing corrosion behavior of silicate glasses. Based on the corrosion mechanisms described and the questions raised in preceding literature, the present study focuses on understanding the corrosion mechanisms governing metaluminous (Na/Al = 1) sodium aluminoborosilicate glasses in acidic environments across a wide composition-space (ranging from SiO_2-rich to B_2O_3-rich compositions), with particular emphasis on understanding the reactions taking place near the glass–fluid interface. Using the state-of-the-art characterization techniques including nuclear magnetic resonance (NMR) spectroscopy, Rutherford backscattering, X-ray photoelectron spectroscopy (XPS) and elastic recoil detection analysis (ERDA), it has been shown that stepwise B_2O_3 substitutions into nepheline ($NaAlSiO_4$) glass, although causing non-linear changes in glass structure network structural features, leads to strikingly linear increases in the forward dissolution rate at pH = 2. While the glasses undergo congruent dissolution in the forward rate regime, the residual rate regime displays evidence of preferential extraction near the glass surface (i.e., enrichment in aluminum content upon corrosion through $AlO_4 \rightarrow Al(OH)_3$ evolution) implying that dissolution–re-precipitation processes may occur at the glass–fluid interface in both B_2O_3-rich and SiO_2-rich glass compositions—albeit with vastly dissimilar reaction kinetics.

Keywords: corrosion; structure; composition

1. Introduction

The chemical durability of glasses may seem like an "old" topic, but its fundamental understanding is of great concern for industry [1, 2] and academia in order to find solutions to the problems relevant to the well-being of humanity and environment.[3, 4] While the majority of literature on glass corrosion is focused on understanding dissolution kinetics and mechanisms of silicate glass chemistries in the neutral–to–alkaline aqueous regime owing to its relevance in the fields of nuclear waste immobilization (where the conditions in geological repository are expected to vary between neutral–to–highly alkaline)[5] and biomaterials (as the pH of the human body fluids varies between neutral to slightly alkaline),[6] understanding the corrosion of silicate-based glass chemistries over a broad composition space in the acidic pH regime is highly important for glass packaging and touch screen electronic display industries. Two important examples in the glass packaging industry where an understanding of acid corrosion is vital are (i) glasses for beverage containment and (ii) glasses for pharmaceutical packaging. The former is important because the pH of the majority of commercial alcoholic or non-alcoholic (non-dairy) drinks ranges from 2 to 7, with a significant portion (>90 %) being at pH < 4.[7] Since many of these drinks are packed in glass bottles/containers, it becomes imperative to understand the corrosion of silicate glasses in acidic environments. Similarly, window glasses are often packed with acidic interleaf materials to buffer against alkaline-pH corrosion during storage, but this acidic material can also facilitate leaching interactions in the presence of moisture.[8] While the majority of the container and window glass industries rely on conventional soda-lime silicate compositions, the glasses used in pharmaceutical packaging are designed mainly in the alkali borosilicate or aluminoborosilicate systems, where these glasses encounter non-neutral pH during their service lifetime.[9] Glasses for display applications also require knowledge of the dissolution behavior of glasses in acidic

environments. For example, cover glasses used as the outer contact surface of touch-screen electronic displays are designed primarily in Na_2O–(K_2O)–Al_2O_3–B_2O_3–(P_2O_5)–SiO_2 systems, where they typically encounter pH varying between 2.5 and 6 (pH of human sweat and skin secretions) during their normal service lifetime.[10] Meanwhile, alkali-free glasses used as the substrates for electronic displays may encounter acidic cleaning chemistries during finishing to remove contaminants that could negatively influence performance of display transistor devices built into the display.

A thorough literature review on the topic of glass corrosion reveals only a handful of studies which discuss corrosion of silicate glasses and their derivatives in the acidic regime—these include only a narrow set of glass chemistries, with most of them being vitrified analogs of SiO_2-rich natural minerals,[11-20] a few being simplified borosilicate-based nuclear waste glasses,[21, 22] and others being on aluminosilicate-based E-glass.[1, 2] Consequently, there is a lack of consensus in the literature on the fundamental mechanisms of glass dissolution in acidic solutions that applies to a wide composition space. For example, according to Gislason and Oelkers,[18] the dissolution of basaltic glasses in solutions (far-from-equilibrium) with pH varying between 2 and 11 is controlled by a single mechanism, which includes (i) release of monovalent and divalent metal cations, (ii) exchange between H^+ in solution and Al in the glass, and (iii) considerably slower removal of silica from the glass. Berger et al.,[20] on the other hand, determined that solution affinity effects play a major role in the dissolution behavior of similar glasses, as their dissolution rates in acidic solutions were found to be driven by surrounding solution concentrations of Al, meanwhile dissolution rate in neutral solutions were similarly driven by aqueous Si concentrations. While the aforementioned studies were able to successfully utilize solution and microstructural analyses to model glass corrosion kinetics in acid according to well-known kinetic theories and draw

conclusions as to dissolution mechanisms, later studies discussed below have incorporated structural and chemical information of the evolving glass surface and bulk to give more insight into the fundamental corrosion mechanisms of silicate glasses in the acidic regime.

Multiple studies by Hamilton et al. .[12-14] looked into the dissolution kinetics of feldspathoid-based sodium aluminosilicate minerals and glasses, including as a function of solution pH, from acidic to basic regimes. These studies correlated the dissolution behavior with glass structural descriptors according to the glass composition—such as the impact of non-bridging oxygen (NBOs) and Si–O–Si vs. Si–O–Al bonding upon ion-exchange / hydrolysis rates near the glass–fluid interface along a specific walk of compositions in the ternary sodium aluminosilicate system. Similarly, Knauss et al.[21] studied a model nuclear waste glass in a range of solution pH, determining that fundamental differences in terms of rate of elemental release and altered layer characteristics (i.e., Si/Al release from the glass) occur as pH rises from acid to neutral environments. Tsomaia et al.[11] expanded upon these findings by performing an in-depth structural study on the surface of sodium aluminosilicate glasses at pH = 2, determining that silicate units are released only after release of Na and Al cations, and provided the first NMR evidence that aluminum tends to form octahedral coordination near the surface, either due to (i) a structural reorganization, involving *in situ* $AlO_4 \rightarrow AlO_5 \rightarrow AlO_6$ transformation or (ii) a re-precipitation mechanism from solution. More recent developments in understanding the kinetics and mechanisms governing glass corrosion—for both acid and neutral-to-alkaline conditions—have attempted to use the latest advances in atomic-scale characterization techniques to generate a unifying model that describes corrosion behavior of silicate glasses, as communicated below.

The most recent literature on this subject debate two basic mechanisms for silicate glass corrosion: (i) the classical multi-step inter-diffusion-based mechanism and (ii) the interfacial

dissolution – re-precipitation mechanism (IDPM).[22] The former describes the mechanism of corrosion as a multi-step process that includes release of mobile glass modifying cations (such as Na^+) through ion exchange with protons in solution to form hydrated Si-OH bonds (forming an inter-diffusion layer), followed by the protonation and hydrolysis of bridging bonds (i.e., Si-O-Si or Si-O-Al) and restructuring of the hydrated silica network into a gel layer via re-polymerization reactions.[23-26] The IDPM, on the other hand, suggests that glass corrosion proceeds as an inward-moving reaction front in which all bonds at the glass–fluid interface break and are immediately re-precipitated to form an amorphous gel layer.[22] The supersaturated water at the interface not only promotes alkali/alkaline-earth release from the glass but in fact releases all elements in the outermost surface layer only to reorganize as a secondary phase of network forming species such as Si and Al.[22] While the classical inter-diffusion-based mechanism has been widely accepted in the glass community, recent studies using highly advanced analytical techniques to track the gel layer characteristics suggest that a basic mechanism describing silicate glass corrosion may be more complicated than assumed in either individual mechanisms, with high dependence upon glass composition and surrounding leaching conditions.[25, 27, 28] Based on previous findings and questions raised in the aforementioned literature, we aim to address the following open questions in our study: (1) What mechanisms best describe the corrosion of alkali aluminoborosilicate glasses in acidic environment? (2) Does AlO_6 gel layer formation in acid occur by way of a structural transformation or re-precipitation? (3) Will the established corrosion mechanisms – multi-step inter-diffusion mechanism or IDPM – accurately describe the dissolution behavior of glasses far from the SiO_2-rich regime, i.e., glasses with B_2O_3 as the primary network former?

In light of the abovementioned questions, the present study is focused on understanding the kinetics and mechanisms of aqueous corrosion of sodium aluminoborosilicate glasses (with

varying B_2O_3/SiO_2 ratio) in acidic solutions (HCl; pH = 2). Accordingly, the glass compositions have been designed in the 25 Na_2O–25 Al_2O_3–x B_2O_3–(50-x) SiO_2 (where x varies between 0 – 50 mol.%) quaternary system. The series of glass compositions were designed to understand the corrosion of oxide glasses with multiple network formers over a broad composition space. The choice of glasses along the metaluminous (Na/Al = 1) join was made with the understanding that alkali cations would, in general, first preferably serve to charge-compensate tetrahedral aluminum in the silicate network [29]. In the absence of "excess" Na_2O beyond the equimolar 1:1 proportion to Al_2O_3, structural complexities such as $BO_3 \rightarrow BO_4$ transformation or Si-NBO formation as a function of composition can be largely minimized, enabling a more direct interpretation of chemical and structural factors driving observed corrosion kinetics. A suite of state-of-the-art spectroscopic characterization techniques including inductively coupled plasma – optical emission spectroscopy (ICP-OES), magic angle spinning – nuclear magnetic resonance (MAS NMR) spectroscopy, X-ray photoelectron spectroscopy (XPS), Rutherford backscattering spectrometry (RBS), and elastic recoil detection analysis (ERDA) have been employed to study changes in the bulk and surface structure/chemistry of corroded glasses as a function of solution chemistry. The results have been discussed taking into account the previously proposed mechanisms for glass corrosion, as discussed in-depth in recent studies, namely in Gin et al.[4] and Geisler et al.[22, 30], alongside the additional literature.[25, 27, 28, 31]

2. Experimental

2.1 Synthesis of the glasses

Glasses in this work were designed along the metaluminous join to maintain charge-balance between Na and Al (i.e., $Na_2O/Al_2O_3 = 1$) while replacing SiO_2 with B_2O_3 in the majority

network, per the composition series 25 Na_2O–25 Al_2O_3–x B_2O_3–(50-x) SiO_2 (in mol. %, where x varies between 0–50 in 5 mol% increments). The silicate endpoint (x = 0) corresponds to the nepheline composition (25 Na_2O-25 Al_2O_3-50 SiO_2), whose dissolution rates have been previously well-studied.[11, 12, 32] All glasses were synthesized using the melt-quench technique, using high-purity powders of SiO_2 (Alfa Aesar; >99.5 %), H_3BO_3 (Alfa Aesar; ≥98 %), Al_2O_3 (Acros Organics; 99 %), Na_2SiO_3 (Alfa Aesar; >99 %) and Na_2CO_3 (Fisher Scientific; ≥99.5 %) as precursors. Oxide precursors were mixed in 70 g batches and melted in Pt-Rh crucibles for 1-2 h in the air at temperatures ranging from 1400-1675 ºC, depending on B_2O_3/SiO_2 ratio in the glass composition. All glasses were quenched on a metallic plate and coarse-annealed at temperatures of T_g^* – 50 °C, where T_g^* is the estimated glass transition temperature obtained from the SciGlass database. Glasses were labeled according to the naming convention "B-x," where x represents the batched B_2O_3 concentration (mol.%). The amorphous nature of the glass samples was confirmed by X-ray diffraction (XRD) (PANalytical – X'Pert Pro; Cu K_α radiation; 2θ range: 10–90º; step size: 0.01313º s^{-1}). The actual concentration of SiO_2, Al_2O_3, and B_2O_3 in the synthesized glasses was determined by ICP–OES (PerkinElmer Optima 7300V), while sodium concentration was determined by flame emission spectroscopy (Perkin Elmer Flame Emission Analyst 200). Table 1 presents the experimentally measured glass compositions. The bulk water content in glasses was estimated from the maxima of the ~3500 cm^{-1} absorption band in the mid-infrared (IR) region, typical of molecular water.[33] The IR spectra were acquired using a single bounce diamond attenuated total reflectance (ATR) apparatus attached to a Fourier Transform Infrared spectrometer (FTIR-UATR, Frontier™, PerkinElmer, Inc.; scanning resolution 4 cm^{-1}, 32 scans for background and samples).

2.2 Glass transition temperature measurements and annealing

Differential scanning calorimetry (DSC) data were collected on the fine glass powders (<45μm diameter) using a Simultaneous Thermal Analyzer (STA 8000; PerkinElmer) from room temperature to 1500 ºC at a heating rate of 20 ºC/min under a constant flow of nitrogen gas. The glass transition temperature (T_g) was deduced from the inflection point of the endothermic dip in the DSC spectra. The T_g values reported in this paper represent an average of at least two thermal scans. After the experimental measurement of the T_g, each glass was re-annealed at a temperature corresponding to their T_g – 50 ºC for several hours and slow-cooled to room temperature until most of the residual stresses were removed, as visualized under a polariscope. A detailed methodology used to anneal the glasses has been described in our previous article.[3]

2.3 Bulk structural analysis of pre- and post-corroded glass samples

The structure of glass (both before and after chemical dissolution) has been studied using MAS NMR spectroscopy. The MAS NMR spectra of ^{27}Al, ^{11}B, and ^{23}Na for glasses and select post-dissolution samples were acquired using a commercial spectrometer (VNMRs, Agilent) and a 3.2-mm MAS NMR probe (Agilent). The samples were powdered in an agate mortar, packed into 3.2 mm zirconia rotors, and spun at 22 kHz for ^{23}Na and ^{27}Al MAS NMR, and 20 kHz for ^{11}B MAS NMR. ^{27}Al MAS NMR data were acquired at 16.4 T (182.34 MHz resonance frequency) using RF pulses of 0.6 μs (equivalent to a π/12 tip angle), recycle delays of 2 s, and signal averaging of 1000 acquisitions. Acquired data were processed without additional apodization and referenced to aqueous aluminum nitrate at 0.0 ppm. ^{23}Na MAS NMR data were collected at 16.4 T (185.10 MHz resonance frequency) using a 0.6 μs (~π/12 tip angle) pulse width for uniform excitation of the resonances. A range of 400 to 1000 acquisitions was co-added, and the recycle delay between

scans was 2 s. The ^{11}B MAS NMR experiments were conducted at 16.4 T (224.52 MHz resonance frequency), incorporating a 4 s recycle delay, short rf pulses (0.6 μs) corresponding to a π/12 tip angle, and signal averaging of 400 to 1000 scans. Similar experimental conditions, but at 11.7 T (160.34 MHz resonance frequency), were used to collect ^{11}B MAS NMR spectra from post-dissolution samples. The acquired spectra were processed with minimal apodization and referenced to aqueous boric acid (19.6 ppm) and aqueous NaCl (0 ppm). Fitting of the MAS NMR spectra was performed using DMFit[34] and, accounting for distributions in the quadrupolar coupling constant, the CzSimple model was utilized for ^{23}Na and ^{27}Al MAS NMR spectra. The "Q MAS ½" and Gaus/Lor functions were used to fit 3- and 4-fold coordinated boron resonances in the ^{11}B MAS NMR data, respectively, and N_4 was calculated from the relative areas of these peaks, with a small correction due to the overlapping satellite transition of the 4-fold coordinated boron peak.[35]

2.4 Sample preparation for glass corrosion tests

2.4.1 Glass powder specimens

The glasses were crushed and sieved to obtain powders with particle size varying between 300 – 425 μm. The glass particles were ultrasonicated in acetone to remove fine powder residue. The process was repeated at least thrice or until the supernatant was clear to ensure the removal of all the fine particles sticking to the surface of larger glass particles. The ultrasonicated glass particles were dried overnight at room temperature in ambient air and analyzed for any structural changes before versus after acetone-washing using FTIR spectroscopy (as has been described previously). Average three-dimensional (3D) geometric surface area of washed particles was determined using ImageJ software (as explained in more detail in Stone-Weiss et al.[3]) after capturing images of ~1000 particles via an optical microscope (Zeiss Axioskop 40) at ~50X

magnification. Experimental density values (measured using Archimedes' method by measuring mass of sample in air and d-limonene solution; number of samples = 3, standard deviation <0.009 g cm^{-3}; presented in Table 1) were used together with 3D surface area calculations to determine the specific surface area of the washed powders (4284-4781 mm^2/g). Finally, the mass of glass particles resulting in the desired surface area–to–volume ratio (SA/V) was calculated.

2.4.2 Monolithic glass coupons

Based on learnings from the corrosion studies of powder specimens, additional corrosion tests were performed on monolithic glass coupons from select compositions (B-5, B-25, and B-45). Two coupons of ~15 mm × 15 mm dimensions were cut from each glass composition using a diamond blade. The polishing of the glass coupons was performed in accordance with the procedure described in the ASTM C1220-10,[36] wherein the glass specimens were ground in acetone sequentially on 120 – 600 grit sized SiC sheets, followed by polishing in a 6 μm non-aqueous diamond suspension until a mirror finish was acquired. The thickness of the polished samples was approximately between 2-3 mm. The dimensions of the polished samples were measured to calculate geometric surface areas.

2.5 Glass corrosion experiments in acidic pH

2.5.1 Dissolution behavior and kinetics of glass corrosion

The dissolution behavior and kinetics of glasses were studied at pH = 2±0.02 (hydrochloric acid; Alfa Aesar; ACS grade) by immersing 27.0 mg of acetone-washed glass particles in 50 mL solution, corresponding to SA/V = 2.5 m^{-1}. All powder–solution mixtures were immediately sealed into sterilized polypropylene flasks and placed in an oven at 35 ºC. Experiments ranged from 5 minutes to 72 hours. In addition to analyses of neat (unused) and blank (glass-free) control

solutions, all experiments were performed in triplicate to evaluate the uncertainty of final results. The pH evolution of the solutions was measured at room temperature from solution aliquots using a pH meter (Mettler Toledo InLab® Pro-ISM). Separate aliquots of the corrosion solutions were chemically analyzed by ICP-OES (PerkinElmer Optima 8300). ICP-OES detection limits were <0.5 ppm for Na, <0.2 ppm for Al, <0.2 ppm for B, and <0.2 ppm for Si. The normalized loss (NL) of each element (Na, Al, B, and Si) released from glasses into the surrounding solution was calculated using equation (1),

$$NL_i = \frac{C_i - C_o}{\left(\frac{SA}{V}\right) f_i} \qquad (1)$$

where C_i is the mass concentration of element i in the solution as detected by ICP-OES; f_i is the mass fraction of the element i in the glass, and C_o is the background concentration (as determined from blank solutions). Normalized loss data were plotted against time and linearly fit over the apparent linear regimes of release at early times to evaluate forward dissolution rates as a function of glass composition and initial solution pH.

2.5.2 Structural transformations in the glasses due to aqueous corrosion

In order to study the mechanism of glass corrosion, both bulk and surface characterization of pre- and post-dissolution glass specimens were performed. The glass powders remaining after dissolution experiments *(from section 2.5.1)* were rinsed thoroughly with water thrice and dried overnight at 65 ºC followed by characterization using XRD and ^{27}Al and ^{11}B MAS NMR spectroscopy. On the other hand, the dissolution experiments on polished monolithic glass coupons were performed at pH = 2 for durations of either 12 hours, 1 day, or 3 days to match the maximum time duration performed with analogous glass grains. Corroded coupons were rinsed with DI water following the dissolution experiments and dried at room temperature to constant weight.

XPS measurements were performed on monolithic glass coupons in order to understand the composition and chemical environment of elements within the top 5-10 nm of the sample surfaces – both before and after corrosion processes. The XPS measurements utilized a Thermo Scientific K-Alpha equipment, which used a 1486.6 eV monochromated Al K_α x-ray source to excite core level electrons from the sample. A low energy dual electron/argon-ion beam flood gun was used for charge compensation during measurements. The kinetic energy of the photoelectrons was measured using a 180° double-focusing hemispherical analyzer with a 128-channel detector. Binding energies were referenced to the main component of the adventitious carbon peak at 284.8 eV. Peak areas were converted to composition using suitable elemental relative sensitivity factors[37] and corrected for attenuation through an adventitious carbonaceous overlayer using a calculation similar to the method described by Smith.[38] The probe depth of XPS, taken to be three times the inelastic mean free path of photoelectrons, varied from 3.6 nm for Na 1s to 9.3 nm for B 1s, Al 2p, and Si 2p photoelectrons.

RBS and ERDA measurements were similarly performed on pre- and post-corroded glass coupons in order to further evaluate the near-surface composition and hydrogen content of the corroded samples, respectively. These measurements were carried out using a General Ionex Tandetron accelerator using a 2.0 MeV He^{++} beam. For RBS, the beam was oriented normal to the sample surface, and the energy of backscattered He ions was measured using a solid-state charged particle detector mounted at 17º to the sample surface normal. For ERDA measurements, the beam was oriented in a grazing geometry with an angle of 75º between the incident beam and the surface normal. The detector was mounted 75º with respect to the surface normal in the specular direction, with a 40 μm mylar foil placed over the active area to block scattered He ions. Hence, only

forward-scattered H ions were able to penetrate the detector. The probe depth of these ion scattering techniques was approximately 1 μm.

3. Results

3.1 Glass formation behavior and annealing

The melt-quenched glasses were transparent in appearance and XRD amorphous (as shown in Figure S1). The experimental compositions, as analyzed by ICP-OES, show close agreement with batched compositions (±1.7 %) (see Table 1). The water content in B_2O_3-containing glasses was estimated to be less than 10 ppm (wt. %).[33]

In order to remove all residual stresses, glasses were annealed at $T_g^{\dagger}$-50 ºC for several hours, followed by slow cooling to room temperature (where $T_g^{\dagger}$ refers to the onset point of the endothermic dip) [3]. Residual stresses in the glasses, as analyzed under a polariscope, were estimated to be less than 10 MPa, taking into account the ~5 mm sample thickness and considering the absence of any first-order fringes under cross-polarized inspection.

3.2 Structural analysis of glasses

The density of glasses decreases linearly as a function of B_2O_3 content, while molar volume displays a linear increase, as shown in Table 1. These trends may be attributed to the introduction of lower bond density BO_3 units (as will be shown by MAS NMR results) into the glass network in place of higher bond density SiO_4 tetrahedra. For this reason, the density of vitreous SiO_2 comprising a tetrahedral silica network is 2.2 g/cm^3, while that for vitreous B_2O_3 with corner-sharing planar BO_3 triangles is 1.8 g/cm^3.[39]

Figure 1a and 1b present the ^{11}B and ^{27}Al MAS NMR spectra of the annealed glasses. ^{23}Na MAS NMR spectra have been presented in Figure S2, and fitting parameters can be seen in Table S1. Since all the glasses studied in this work have been designed in the metaluminous regime (Na/Al = 1), we expect sodium to act in a charge compensating role to either AlO_4^- or BO_4^- network forming units, in preference to being used to form NBOs in the silicate network (i.e., silicate units are expected to be entirely Q^4). Studies have shown that aluminum tends to preferentially consume Na^+ relative to boron in SiO_2-rich alkali aluminoborosilicate glasses.[29, 32, 40, 41] However, it has also been shown that Al-vs-B competition for sodium may shift away from Al in favor of B more significantly in B_2O_3-rich glasses.[42, 43] ^{11}B NMR spectra shown in Figure 1a display two main resonances: a broad quadrupolar-broadened peak centered at 14 ppm associated with BO_3 units, and a minor, relatively narrow peak centered at 2 ppm associated with BO_4 units. The BO_3 peak does not show any significant change in shape with increasing *x*, implying that ring vs. non-ring BO_3 species maintains similar ratios in the network. While the BO_4 peak mentioned is not clearly evident in SiO_2-rich glasses, this peak becomes more prominent as *x* increases beyond 20 mol.% depicting an increasing concentration of BO_4 units in the glasses with increasing B_2O_3. Table 2 presents the N_3 and N_4 fractions in glasses as calculated from the fitting of ^{11}B MAS NMR spectra. The highest N_4 fraction of 6% was observed in the sodium aluminoborate glass (*x* = 50). It is important to note that any BO_4 units shown (experimentally) to develop in the structure of a metaluminous glass must consume Na^+ in its need for charge compensation, which consequently is expected to impact Al speciation in the network. In order to explore this, we also examined ^{27}Al MAS NMR spectra (shown in Figure 1b). At low B_2O_3 content, these spectra display the main resonance centered near 60 ppm (associated with AlO_4) and a very minor peak near 0 ppm associated with a background rotor signal. The AlO_4 peak shifts towards higher shielding with

increased B_2O_3 content, which we attribute to a systematic shift in next-nearest-neighbor identity as Al-O-B bonds begin to replace a predominantly Al-O-Si bonded network.[44] In keeping with trends in the ^{11}B MAS NMR spectra of B_2O_3-rich glasses, clear changes also occur in ^{27}Al MAS NMR spectra of B_2O_3-rich glasses, wherein, the development of a peak near 30 ppm associated with AlO_5 is evident. Table 2 presents the amount of 4- and 5- coordinated Al present in the glass network as deduced from the ^{27}Al MAS NMR spectra. While glasses with up to x = 30 show aluminum predominantly in tetrahedral coordination (98-99 %), increase in B_2O_3 concentration beyond 30 mol. % leads to a steady rise in AlO_5 content up to 6 % in the sodium aluminoborate glass (x = 50), thus, deviating from its expected tetrahedral role in metaluminous glasses. Although the existence of five-coordinated aluminum units in metaluminous and per-aluminous glasses or glasses with high ionic field strength cations has been widely reported,[43, 45-48] its role in the structure—i.e. network former vs. network modifier—and properties of these glasses is still disputed. While higher (five- or six-) coordinated aluminum is conventionally considered to act as a network modifier,[49, 50] the presence of AlO_5 units in the glass structure has been shown to result in an increase in their glass transition temperatures, melt viscosity, and hardness.[43, 50-54] Interestingly, in our study, with increased B_2O_3 content, the fraction of higher coordinated Al and tetrahedral B units both rise, deviating from the expectation that aluminum tends to preferentially consume Na^+ for the charge compensation of AlO_4^- before boron can use them to convert BO_3 to BO_4. It is evident that in B_2O_3-rich (molar concentration of $B_2O_3 > SiO_2$) metaluminous glasses, the tetrahedral boron units begin to 'steal' Na^+ away from network forming Al units and cause higher-coordinated Al species to form.

In order to assess sodium's role around oxygen and verify the connectivity of the silicate network, we used analyzed compositions and the NMR-determined AlO_4 and BO_4 fractions to calculate NBO fractions, per the formula:

$$NBO\ Fraction = \frac{at.\%\ Na - at.\%\ B\ in\ BO_4 - at.\%\ Al\ in\ AlO_4}{at.\%\ O} \qquad (2)$$

In this formula, we assume that one Na^+ forms either one BO_4 or one AlO_4 unit, and that any excess alkali will begin to form NBOs in the silicate network on a 1-for-1 basis.[55] The results of these calculations have been presented in Table 2. It is important to note that, in this assumption, we have not taken into account AlO_5 units due to their small concentrations and uncertainties concerning their impact on the NBO content in the glass network. It is evident from these calculations that, in each composition, the network contains less than 0.1% of NBOs, thus verifying sodium's primary role as a charge compensator, as well as the anticipated high connectivity of these glasses marked by Q^4 silicate structural units.

3.3 Glass structure vs T_g

In general, an increase in the B_2O_3 concentration in the studied glasses, at the expense of SiO_2, resulted in a significant reduction in their glass transition temperatures, as shown in Table 1. However, the variation in T_g with increasing B/(Al+Si) molar ratio is non-linear, as is evident from the close agreement between a fitted exponential function and the experimental data (as shown in Figure 2a). Since Na/Al = 1 in all batched compositions, it is expected that a variation in the B_2O_3/SiO_2 ratio will result in a decline in T_g since tetrahedrally coordinated SiO_4 units will be replaced by less-constrained BO_3 units, leading to an overall reduction in network rigidity. However, the non-linear decrease in T_g shown with increasing B_2O_3 content in glasses is intriguing and maybe explained based primarily on the following two viewpoints: (i) a gradual shift in the

network topology with varying B_2O_3/SiO_2 ratio as tetrahedrally coordinated aluminosilicate glass network is being gradually converted to an aluminoborate network where trigonal BO_3 replaces tetrahedral SiO_4 as the main network forming unit, and (ii) an increasing average aluminum- and boron- coordination in the glass structure (in $x \geq 25$ compositions).

The first viewpoint can be argued according to Figure 2b, which displays the percentage breakdown of the glass network into its constituent glass-forming species (normalized to 100 %). In the studied system, where we anticipate having negligible NBO content, this breakdown represents a comprehensive depiction of the glass network evolution in a series of fully polymerized glasses. It is shown that while tetrahedral Al and Si are present in near-identical quantities at $x = 0$ (nepheline composition), the substitution of B_2O_3 for SiO_2 leaves AlO_4 as the primary network component from $x = 5$ to $x = 20$, beyond which BO_3 units exist as the main network constituent ($x \geq 25$). The shift along this series from networks rich in tetrahedral Al and Si species to those rich in trigonal B contributes to a network with fewer constraints and higher degrees of freedom, thus contributing to gradual decreases in T_g.[56] However, it can also be noted in Figure 2b that concentration of SiO_4 and BO_3 units in the glass structure changes in a non-linear fashion as a function of B/(Al+Si) ratio, similar to what is seen for T_g in Figure 2a. For instance, although SiO_4 fractions initially reduce with a steep negative slope, the magnitude of the negative slope gradually decreases (as evidenced by ~30 % reductions from $x = 0$ to $x = 25$ and ~20 % reductions between $x = 25$ and $x = 50$). BO_3 unit fractions, on the other hand, first rise with a steep positive slope, which continuously reduces as a function of B/(Al+Si) ratio. Thus, the non-linear trends in the variation of both SiO_4 and BO_3 network fractions may help to explain the non-linear decrease in T_g with increasing B_2O_3/SiO_2 ratio.

The second possible explanation for the non-linear trend observed in T_g is the rise in average Al and B coordination, especially in glasses with $x \geq 25$ mol. %. As evident from the secondary y-axes of Figure 2a, the average aluminum and boron coordination (hereafter referred to as <Al> and <B>, respectively) varies between 4.01-4.02 and 3.00-3.02, respectively in glasses with $x \leq 25$ mol.%. However, <Al> and <B> increases from 4.01 to 4.06 and 3.02 to 3.06, respectively, with increasing B_2O_3 content in glasses with $x \geq 25$ mol.%. It has been well documented in the literature that rising BO_4 content leads to an increase in the glass network rigidity and a corresponding increase in T_g values.[3, 57] However, uncertainty with respect to the impact of <Al> upon network rigidity may be addressed based on the T_g and structural data of glasses in the composition system 20 Na_2O–y Al_2O_3–(80-y) B_2O_3 (y varies between 5 – 25 mol.%) as reported in our previous publication.[43] The ^{11}B and ^{27}Al MAS NMR results on sodium aluminoborate glasses in our previous article had highlighted a decrease in the N_4 fraction from 24 % (y = 5) to 8 % (y = 25), and for AlO_4 fraction from 98 % (y = 5) to 73 % (y = 25) as shown in Figure S3a. Ideally, the decreasing N_4 and AlO_4 fractions should suggest decreasing connectivity in the glass network and, thus, a reduced T_g. However, the T_g in these glasses was observed to increase with an increasing concentration of Al_2O_3, as has been shown in Figure S3b. This was explained to occur due to a rising fraction of five-coordinated aluminum in the glasses from 2 % (y = 5) to 23 % (y = 25), thus, increasing <Al> from 4.0 to 4.3. Similar results have been reported in the case of glasses in the Li_2O–Al_2O_3–B_2O_3 system[45] and several alkali and alkaline-earth aluminosilicate glass systems.[54] As discussed earlier, though the role of five-coordinated aluminum in the glass structure is still disputed, these findings indicate that AlO_5 units have a reticulating effect on the glass network. Thus, based on our previous results and the existing literature, the rise in <Al> in glasses with $x \geq 25$ mol. % (due to the formation of five-coordinated

aluminum) in the present study may also be a contributing factor (along with the non-linear variation in SiO_4 and BO_3 units) to the non-linear variation in T_g.

3.4 Chemical dissolution behavior

3.4.1. Forward rate regime – Dissolution kinetics and solution analysis

Table S2 presents the pH, elemental concentrations, and normalized mass loss (NL) data for the glasses in this study as a function of time, while Figure 3a-e displays NL vs. time curves for compositions B-0, B-5, B-25, B-45, and B-50, respectively. The data points at each timestep represent an average elemental concentration from two duplicate experiments, and where the liquid aliquot from each experiment was measured three times by ICP-OES. In an attempt to capture the early release behavior, experiment durations were varied depending on the relative durability of each glass composition. The release of Na^+ cations and Al species occurs readily in acidic solutions due to ion-exchange / hydrolysis,[13] and has varying effects upon drift of solution pH from its initial value: Na^+ released from a glass tends to increase the alkalinity of solution, while alumina species (which exist as Al^{3+} or $Al(OH)_3$ in acidic environments) exhibit amphoteric behavior, depending on the acidity of solution and relative concentrations of Al species.[58, 59] Meanwhile, the release of B—a species which is also released at elevated rates—has an opposite effect on the pH as its extraction is tantamount to additions of boric acid to the solution. Beyond the initial buffering capacity of the pH = 2 solution imposed by the 0.01 M HCl concentration, the pH of a solution is thus subject to drift in accord with the concentration of elements released over time, and further moderated by the balance of different elemental species released as a function of glass composition (e.g. Na vs Al vs B). The spread of pH values over time is captured in Figure 4, which plots measured solution pH as a function of glass composition (via batched B_2O_3 content); corresponding pH data are listed in Table S2. Dissolution experiments with an initial pH of 2 show

a steady rise in pH over time, with ultimate values trending between 2.2-2.5. The spread of pH data in Figure 4 helps to additionally demonstrate the impact that glass composition has upon pH evolution, where 12 h time durations have been highlighted in a different color. It can be seen that while B_2O_3-rich compositions reach higher pH values within 12 h than SiO_2-rich counterparts, all compositions show pH change of less than ±0.3 within the same time duration, demonstrating the reasonable buffering capacity of pH = 2 solutions, and thus enabling assessment of acid dissolution behavior without the complication of more significant pH drift during a given experiment.

We utilized the curves shown in Figure 3 to compare the release kinetics between different elements and calculate forward dissolution rates for each composition, while also gaining relevant information related to the dissolution mechanisms of these glasses in acidic media. Acidic environments tend to promote ion exchange/hydrolysis of the glass network relative to solutions with near-neutral pH, in this case with normalized loss values at pH = 2, reaching upwards of 100 g/m^2 within the first 12 hours of experiments. This tendency for rapid attack of the network is especially prominent in glasses with significant Al_2O_3 content, as Al-O bonds tend to undergo rapid hydrolysis in acids relative to neutral pH conditions.[24] In the studied acidic environment, we see in Figure 3 that all glasses show (i) an initial linear increase, followed by (ii) a concave downward behavior indicative of decreases in elemental release rates towards a slower residual rate. The reduction in apparent release rate in static experiments can result from several possible mechanisms, including formation of a protective gel/precipitate layer near the surface of the glass or solution feedback effects that manifest as elements approach saturation in the surrounding aqueous environment (we will explore this in more depth in the next section as we discuss residual rate).[24, 26] From the NL data, it can be seen that SiO_2-rich compositions showed nearly 100 g/m^2 release in 72 h, while B_2O_3-rich compositions in the same environments saw this same magnitude

of release in only 12-24 hours. In terms of elemental differences in release behavior, all glasses tend to show close agreement between NL values of Na, Al, B, and Si within the forward rate regime, implying congruent release behavior. These similarities will become more apparent as we compare forward release rates and discuss experimental uncertainty.

Statistical uncertainty reported for each normalized loss point has been determined as 1σ standard deviation for duplicate samples; propagated uncertainty of corrosion experiments has also been calculated, and these values approach as high as 50-60 % of the mean value. While standard deviation calculations only consider data from duplicate experiments and may need confirmation using larger sample sizes, propagation of uncertainty aims to encapsulate all systematic experimental uncertainties and estimate their combined sum—in our case, the vast majority arising from uncertainty in particle surface area. Since the vast majority of our NL standard deviations lie within 20 % of the mean value and NL/forward rate uncertainties typically seen in literature are less than 15-25 %[60-62] (for crushed glass in static conditions, using geometric SA, especially in high rate conditions), the propagated uncertainty we have calculated may overestimate uncertainties which arose from spherical approximations of crushed particles. Thus, we expect measured uncertainties from replicate experiments in our study to provide comparable estimates of total uncertainty and will consider this amount of uncertainty when evaluating NL data in our dataset.

In order to further compare release kinetics for these glasses, we deduce forward dissolution rates based on each element by performing linear regression on normalized loss vs. time plots in the early, linear portions of the release curves (within the first 3-12 hours). The slope of the line provides an estimate of the forward dissolution rate; these fits should only be considered estimates due to the somewhat subjective nature of determining the linear portion of the NL curve,

as well as observing non-zero intercepts at t = 0 (with fits not being constrained to pass through (0,0)). Experimental error in fitting a single dissolution rate to NL data has been highlighted extensively in the literature.[63, 64] Rates and uncertainties, according to B_2O_3 content (and B/(Al+Si) molar ratio) can be found in Table 3. In order to assess standard uncertainty in linear regression, the standard deviation of each NL data point was considered, and the relative impact of fitting a slope to uncertain data was summed to determine the overall fitted-slope uncertainty, similar to the method discussed by Kragten.[65] Normalized loss rates based on each element varied between 3 – 18 g m^{-2} h^{-1}, showing a steady increase with increasing B/(Al+Si) ratio, as illustrated in Figure 5. This rate increase across the series was expected due to borate network incorporation. However, its relatively linear behavior according to B/(Al+Si) ratio (as seen in Figure 5) is a striking result considering the non-linear behavior observed in T_g and network structure (Figure 2). The non-linear trend detected for T_g has earlier been ascribed to either (i) shifts in network topology due to replacement of tetrahedral species (i.e. AlO_4 and SiO_4) by BO_3 or (ii) increases in coordination of both Al and B. The trends observed imply that although compositional evolution in the studied system impacts glass network connectivity and short-ranged structure, NL rates are relatively insensitive to these changes. Instead, we see that dissolution rates generally undergo linear variation according to B composition in the glass, indicating that B_2O_3-for-SiO_2 network former substitution promotes incremental changes in chemical durability.

In terms of elemental release comparisons, we see that while some glasses have deviations of up to 20-35 % between the NL rates of different elements, the studied glasses show a general NL rate similarity between Na, Al, B, and Si (where present in the glass), indicative of an apparent congruent release in the forward rate regime when subjected to acidic environments. Slight differences in release rates may arise due to uncertainties typically estimated from dissolution

experiments and the challenges with estimating forward rates from NL curves—surface-sensitive experiments discussed later in this text will further explore release trends during the residual rate regime and aim to validate our kinetic observations near the glass–fluid interface.

3.4.2. Residual rate regime – Glass structural transformations due to aqueous corrosion

Although we see from the estimated dissolution rates that the glasses dissolve congruently in the forward rate regime, NL values for B in the majority of the compositions (x = 5 – 35) lie below Al, Si and/or Na at longer time durations in these experiments (12 – 72 h)—a time window taken to represent the residual rate regime. In order to further explore the structural and compositional changes taking place near the glass surface in this regime, recovered glassy grains, and bulk coupons were analyzed using multiple bulk and surface characterization techniques.

Grains recovered from the dissolution experiments were analyzed via XRD and MAS NMR to obtain insight into the structural evolution of glasses during corrosion. XRD analysis determined all grains recovered from experiments to be amorphous, ruling out the formation of significant crystalline secondary phases during corrosion. Meanwhile, ^{27}Al and ^{11}B MAS NMR were performed on selected samples, and results are summarized in Figures 6a and 6b. We chose to analyze grains obtained after the final timestep of corresponding static experiments, focusing on glass compositions B-0, B-25, and B-50—the goal being to investigate extremes of potential structural changes taking place as glasses across the composition series corrode. Figure 6a displays the ^{27}Al MAS NMR spectra of pre- and post-corroded glasses. In this figure, we see that B-0 and B-25 glasses show identical ^{27}Al spectra before versus after corrosion. The position of the peak corresponds to Al in a tetrahedral environment, and the consistency of the spectra indicates that the local environment around Al is not detectably altered in these glasses during corrosion. In the composition B-50, on the other hand, while the AlO_4 and AlO_5 peaks appear identical before and

after corrosion, development of a noteworthy peak near 5 ppm can also be seen after 12 h of corrosion. We associate the emergence of this peak with the development of hydrated AlO_6 secondary phases near the glass–fluid interface.[11, 43, 66] The breadth of the AlO_6 peak in the ^{27}Al MAS NMR spectra is indicative of an amorphous phase (corroborated by XRD), whereas crystalline $Al(OH)_3$ has been shown to form during corrosion of aluminoborate glasses in near-neutral–to–alkaline pH conditions due to significant decreases in alumina solubility.[43] It should be noted here that, despite significant amount of dissolution in samples from both SiO_2-rich and B_2O_3-rich glass compositions at pH = 2, the formation of AlO_6 units was observed only in the sodium aluminoborate end-member sample (B-50). Although the formation of AlO_6 units in aluminosilicate glasses has also been reported in the literature (when corroded in acids for long durations),[11, 66] our finding that AlO_6 only forms in B_2O_3-rich compositions (within the studied time durations) is attributed to the faster dissolution kinetics of aluminoborate glasses in comparison to their silicate analogues, which engenders a more rapid approach to corresponding solubility limit(s) within the timeframe of the experiment.

Figure 6b presents the ^{11}B MAS NMR spectra of B-25 and B-50 glasses after corrosion. These data were obtained at the lower magnetic field than those for the pre-corroded glasses in Figure 1a, inhibiting direct spectral overlay due to known changes in peak shape with magnetic field. That said, when comparing the quantified results from Figure 6b to those from the pre-corroded glasses, calculated N_4 fractions are almost identical (± 0.5 %; within ± 0.5 % error limits typically associated with fitting MAS NMR spectra). This indicates an insignificant degree of structural change in the borate glass network (irrespective of the glass composition) during corrosion, as well as implying little to no precipitation of hydrated boron species from solution on the glass surface in this residual rate regime. Thus, acidic environments attacking the borate glass

network seem to hydrolyze bonds with no preferential affinity for hydrolysis of BO_3 or BO_4 units despite differences in their typical bond energies.[43] While we have not discussed the silicate network, we expect silicate units in contact with acid to act in one of two ways: (i) hydration of Si-O bonds (Si-OH) or (ii) rapid apparent release of Si due to silicate "cluster" release following hydrolysis of the surrounding Al or B network, as network connectivity decreases significantly.[12, 67-69] As mentioned in the previously proposed mechanisms for glass dissolution,[4, 22, 30] ultimate gel layer formation can occur through either method via precipitation of partially bonded or free species at the glass – acid reaction front.[22, 70] Surface analysis techniques will better explain the mechanism of silicate-acid interactions taking place.

Based on the NL results from glass grains, the polished coupons of glasses B-5, B-25, and B-45 were corroded in HCl (pH = 2) solutions for 3 days, 1 day, and 12 hours, respectively, creating samples with surfaces representative of the residual rate regime. The pre- and post-corroded glass coupons were analyzed using surface sensitive techniques. XPS spectra for the pre- and post-corroded B-45 samples are shown in Figure 7, and the corresponding elemental compositions (for B-5, B-25, and B-45, both pre- and post-corrosion) are summarized in Table 4. The measured surface compositions of the as-polished samples agree reasonably well with the bulk experimental compositions (as analyzed via ICP-OES) except for the B content of sample B-5, which shows a 2.5× enrichment at the surface. As this discrepancy is well outside the expected statistical error in the XPS measurements, this can be possibly attributed to slight segregation of B_2O_3 at the surface of the sample.

Upon exposure to acidic environments, the composition of sample B-5 was relatively unchanged in the surface layer, reverting largely to the composition expected from that of the bulk glass. However, samples B-25 and B-45 both showed moderate to a significant reduction in their

Na and B content. The surface of sample B-45 was almost entirely depleted in Na and B (80-90 %), while a factor of ~2.4 enriched Al after immersion. In Figure 7a, it is evident that while the polished Al 2p peak lies near 74.2 eV, the corroded sample shifts towards slightly higher binding energy (74.8 eV). This shift could indicate the presence of octahedral $Al(OH)_3$ units, as examined in Refs.[71-73], and may further correspond with a gradual shift in Al speciation from 4- to 6-coordination seen in MAS NMR of B-50 post-corroded grains.[74] O 1s spectra, meanwhile, show a significant change between pre- and post-corroded samples due to likely changes in mixed network former linkage ratios (for example, Al-O-B, B-O-B), as well as surface hydration effects, during corrosion. At these spectral resolutions, we also cannot rule out the possibility of the formation of NBOs near the surface due to bond hydrolysis (which typically contributes intensity near 531 eV).[75, 76] Difficulties with deconvoluting the numerous species contained within the O1s peak of oxide glasses are well-documented, and thus no attempts to further quantify these effects have been made here.

The RBS spectrum of sample B-45 (polished and corroded) is shown in Figure 8a and measured elemental compositions of B-5, B-25, and B-45 before and after corrosion are displayed in Table 5. Note that the RBS spectrum of corroded B-45 glass has been shifted downward to line up the intensities of the Al/Si onsets for ease of comparison. As a reminder to the reader, RBS measurements probe depth of about 100-300 nm and thus are expected to probe an information depth significantly further into the surface than in XPS. It can be seen that RBS-measured surface and bulk experimental compositions agree well in the polished samples. RBS results for the corroded samples, meanwhile, suggest that only the composition of sample B-45 changed significantly beyond the XPS-measured surface layers, as the loss of Na extended well into the RBS-measured depth of the surface. Additionally, Al in B-45 was enriched by ~66 % in the bulk

of the corroded sample as compared to the polished sample, implying that the Al enrichment in this sample may extend to a depth beyond that probed by XPS. Samples B-5 and B-25 showed no statistically significant changes in the bulk.

The ERDA spectrum shown in Figure 8b indicates that sample B-45 absorbed a significant amount of hydrogen upon exposure to acidic solutions, reaching a hydrogen content of 33% within the top 1 μm of the glass. The remaining samples showed only background levels of hydrogen both before and after immersion (see Figure S5). Note that the samples charged slightly during these measurements due to their relatively low conductivity and hence the energy onset of the surface peak was not consistent.

4. Discussion

The aim of this study was to address the open questions: (1) What mechanism(s) best describe the corrosion of glass in acidic environments? (2) Specifically, does AlO_6 gel layer formation in acid occurs by way of a structural transformation or re-precipitation? (3) Will the established corrosion mechanisms – multi-step inter-diffusion mechanism or IDPM – accurately describe the dissolution behavior of glasses far from the extensively-studied SiO_2-rich compositional regime (i.e. B_2O_3-rich samples)?

In order to achieve this goal, we employed several state-of-the-art techniques to characterize the evolution of solution, bulk and surface chemistry, and structural features in glass samples after aqueous corrosion. We found that acid submersion (pH = 2) of sodium aluminoborosilicate glasses extending from silicate- to borate-rich endmembers resulted in a range of glass responses as were manifested in the elemental release behavior from the glass and structural/compositional modifications observed near the glass–fluid interface. As the batched

glasses were designed in the metaluminous (Na/Al = 1) regime, Na^+ in the network was expected to play a charge compensating role for primarily AlO_4 and possibly BO_4, thus maintaining full connectivity of the silicate network. Furthermore, as high overall connectivity was maintained in these glasses (Table 2 estimates NBO fractions in each glassy network), the structural drivers for network corrosion are anticipated to be highly dependent upon medium-range order characteristics (i.e. Si-O-Al, Si-O-B, B-O-Al linkages), where composition and network former ratios play a major role in defining the extent of network mixing thus greatly affecting the rate of network hydrolysis and elemental release.

We particularly expected relative fractions of BO_3/BO_4 and AlO_4/AlO_5 species in the network to greatly affect network mixing characteristics in the studied compositions, which may be governed by stoichiometric mixing or by coordinated 'tetrahedral avoidance' rules, where bonds such as $Al^{[4]}$-O-$Al^{[4]}$ or $Al^{[4]}$-O-$B^{[4]}$ are generally avoided in the glass network.[40, 48, 77, 78] In our system, we see in Table 2 that silicate-rich glasses show almost exclusively BO_3 and AlO_4 structural units (>98 %) with a completely polymerized silica backbone (~4 BO per tetrahedron), which is consistent with previous studies of similar mixed network former compositions.[32, 40] However, as we enter the borate-rich region, we begin to see steady replacements of BO_3 and AlO_4 by BO_4 and AlO_5, respectively, up to ~6 % of each in the aluminoborate endmember glass, the trend of which has also been previously observed in similar aluminoborate glasses.[44, 79] In terms of medium-range order, it has been observed that nepheline ($NaAlSiO_4$) glasses tend to form a highly interconnected aluminosilicate network, with roughly 4 bridging oxygens per Si tetrahedron connecting to Al.[12, 48] As we introduce B_2O_3 for SiO_2, Si-O-B and Al-O-B bonds begin to replace the highly linked Si-O-Al network until the $NaAlB_2O_5$ endmember, where we expect an Al-O-B and B-O-B linked glassy network.[44] We deduce from Figure 2a and 2b that although T_g decreases

along the series due to the replacement of tetrahedral Al and Si units by less-constrained BO_3 units, the non-linear behavior of T_g (and network rigidity) is impacted either by the similarly non-linear evolution of the network former fractions (i.e. BO_3 substitution for SiO_4 and AlO_4; Figure 2b) along the glass series, or by an increase in aluminum and boron coordination (i.e. rises in AlO_5 and BO_4; Figure 2a) in B_2O_3-rich compositions ($x > 25$), which we have described strengthening the glass network. In the following section we explore the influence changes in network structure can have on glass corrosion.

Glasses exposed to acidic solutions tend to undergo the process of ion exchange and hydrolysis at accelerated rates relative to neutral-pH solutions. Furthermore, due to the high Al solubility in acidic media, nepheline-based glasses will degrade quickly in acid due to the rupture of Al-O-Si bonds, which constitute the network. In tandem with H^+/H_3O^+ penetration to extract Na^+ from the glass, hydrolysis of Al-O bonds, and subsequent release of Al^{3+} cations—species which previously held together isolated Si tetrahedra—will cause the network to degrade, leading to the rapid release of silicate units as silicic acid.[12] As B_2O_3 is substituted into the network in place of SiO_2, the introduction of more readily-hydrolyzed Al-O-B and Si-O-B linkages drives network hydrolysis to occur at a faster rate in comparison to Si-O-Al.[80] In Figure 5 and Table 3, we see that, in acidic environments, increasing B/(Al+Si) ratio in the glass leads to a general linear increase in forward dissolution rates by a factor of 4-6× proceeding from aluminosilicate to aluminoborate endmembers, despite non-linear evolution of the glass network structure and rigidity.

Comparing inter-elemental release patterns from the various glass compositions, we observe that acid attack leads to congruent release in the forward rate regime, as displayed by NL curves for Na, Al, B, and Si NL and the estimated forward rates being within the experimental

error of one another during the initial stages of dissolution (Figures 3 and 5). While previously reported findings suggest that silicate glasses in acid media dissolve congruently,[11, 14, 21, 30] our results show that as B is added, signs of apparent incongruency emerge, and are especially evident in the residual rate regime of SiO_2-rich glasses as B release drops below that of Al, Si, and/or Na. In order to supplement our understanding of the elemental release mechanisms occurring at the glass–fluid interface in the residual rate regime, surface compositional and structural changes were uncovered by using a combination of multiple characterization techniques.

Although XRD studies of recovered grains detected that corroded glasses lacked significant crystalline secondary phases, the combination of MAS NMR and XPS / RBS / ERDA techniques enabled us to gain additional insight into the amorphous structural and chemical changes occurring near the glass–fluid interface. Through MAS NMR experiments, we observed that while B coordination in all glasses shows negligible changes, Al in B_2O_3-rich glasses begins to undergo a coordination change from predominantly AlO_4 to AlO_6, as determined from the development of a peak near 0 ppm in B-50 (as seen in Figure 6a) following corrosion. XPS studies corroborate these results by a marked enrichment of atom% Al and potential indications of AlO_6 units after 12 h of acid corrosion in B-45, as implied by a significant shift in the Al 2p peak towards higher binding energy,[71, 72, 74] and accompanied by the development of an O 1s peak likely associated with NBO (see Figure 7). An intriguing outcome of XPS / RBS experiments in the same sample (B-45) resides in that the following observation: Even though we have seen Al elemental release occur at similar rates to B in these experiments, as Na and B are significantly depleted (80-90 %) in the top ~10 nm, we see Al enrichment at the surface by a factor of ~2.5 in the top ~10 nm (XPS) and a factor of ~1.5 in the top 100-300 nm (RBS) (presumably in a hydrated 6-coordinated form; see Table 4 and 5). ERDA performed on this sample confirmed the presence of H as either H^+/H_3O^+ or diffused

H_2O species within the top ~1 μm of the glass surface. We should also note that Al enrichment and Na / B depletion from the surface were also seen in the B-25 (SiO_2 / B_2O_3 = 1) composition, although to a much less extent. Studies by Tsomaia et al.[11] and Criscenti et al.[66] in sodium aluminosilicate glasses at pH = 2 had previously determined that an enriched AlO_6 layer forming at the glass–fluid interface occurs upon corrosion by way of structural transformation at the glass surface. However, in our studied borate-rich glasses, we can alternatively explain the Al enriched surface formed either by a re-precipitation or adsorption process of Al species from solution following significant degradation of the borate network, which agrees with literature showing that dissolved Al exists in an octahedral form.[11, 66] Thus, regardless of elemental release trends which seem to signal that the glass corrodes in a congruent fashion with regards to Al, we determine that these glasses begin to undergo a re-precipitation/gel layer formation mechanism on approach to the residual rate regime, even when silica is not present in significant amounts in the initial glass structure.

Our findings tend to show consistency with what was proposed by Geisler et al.[22] for experiments performed with a simplified glass composition at pH 0, which suggest that glass dissolution proceeds as an inward moving reaction front, where all elements are released congruently, followed by the formation of a re-precipitated gel layer. However, we are seeing an apparent shift in corrosion mechanism between SiO_2-rich and B_2O_3-rich samples, marked by the differences seen in the surface layers of borate-rich samples (in the form of an AlO_6-rich hydrated layer)—while SiO_2-rich glasses ($x \leq 25$)—which undergo similar magnitudes of normalized loss—do not show clear evidence of hydrated layer formation. Aluminum in octahedral coordination near the surface of nepheline-based glasses, which has been found in glasses corroded at pH = 2 for more extended time durations (near 1000 h),[11] may only occur in the latter stages of dissolution

in which silica is saturated in solution and more significantly depleted from the glass–fluid interface. By comparison, in B_2O_3-rich samples, hydrated AlO_6 layers begin to form at the surface following degradation of the borate network, which occurs at an accelerated rate. Presumably, this breakdown promotes a dissolution–re-precipitation mechanism at the surface, as Al has been shown to release from the glass at similar rates to other network formers as opposed to remaining in the glass. Sodium aluminoborosilicate glasses dissolving in acidic conditions tend to act in ways that reflect their medium-range order, and we have also shown that—while composition plays a clear role in the reaction kinetics and mechanisms occurring at the glass–fluid interface—recently proposed mechanisms for glass corrosion may provide the basis for understanding the way a wide range of glass compositions (extending into the B_2O_3-rich region) corrode under acidic conditions. Further examination of the pristine glass/hydrated layer interface, for instance through high-resolution depth profiling (i.e. TEM, ToF-SIMS, etc.), would provide valuable supplemental information about the molecular scale mechanisms and drivers governing corrosion of these glasses in acidic environments.

5. Conclusions

The current study has attempted to understand the mechanisms governing corrosion of glasses in acidic environments. Accordingly, a series of glasses in the 25 Na_2O–25 Al_2O_3–x B_2O_3–(50-x) SiO_2 (x varies between 0 and 50 mol. %) was subjected to pH = 2 environments where the evolution of solution, bulk and surface chemistry, and structural characteristics of glass were studied using a suite of state-of-the-art spectroscopic characterization techniques. It has been shown that, although stepwise addition of B_2O_3 into the glass causes non-linear changes in network structural characteristics—i.e. T_g and fractions of AlO_5/BO_4 in the glass—noticeably linear

increases in the forward dissolution rates are observed. As has been seen in previous literature for SiO_2-rich compositions, we observed that glasses submerged in acid underwent an apparent congruent release in the forward rate regime. In the residual rate regime, however, deviations from congruency were detected, as Al enrichment through $AlO_4 \rightarrow Al(OH)_3$ evolution was observed at the surface of corroded B_2O_3-rich glasses. When comparing our results to the existing literature, the findings imply that dissolution–re-precipitation processes occur at the glass–fluid interface in both B_2O_3-rich and SiO_2-rich glass compositions, notwithstanding vastly different reaction kinetics. The present investigation forms the basis for further study of the glass surface in wide-ranged glass compositions, as further implementing atomic-scale depth profiling can better probe the reactive interface and help to pinpoint molecular mechanisms governing aqueous corrosion.

Acknowledgment

This material is based upon work supported by the National Science Foundation under Grant No. 1507131, the US Department of Energy (DOE) – Offices of Nuclear Energy and Environmental Management through Nuclear Energy University Program under Grant No. DE-NE0008597, and US DOE – Office of River Protection under Grant No. DE-EM0003207. ORNL is operated by UT-Battelle, LLC, for the US DOE under Contract No.'s DE-AC05-00OR22725. The authors also thank the Characterization Sciences group at Corning Incorporated for compositional analysis of the glasses.

References

1. Q. Qiu and M. Kumosa, *Compos. Sci. Technol.*, 1997, **57**, 497-507.
2. R. Jones and J. Stewart, *J. Non-Cryst. Solids*, 2010, **356**, 2433-2436.
3. N. Stone-Weiss, E. M. Pierce, R. E. Youngman, O. Gulbiten, N. J. Smith, J. Du and A. Goel, *Acta Biomater.*, 2018, **65**, 436-449.
4. S. Gin, A. Abdelouas, L. J. Criscenti, W. L. Ebert, K. Ferrand, T. Geisler, M. T. Harrison, Y. Inagaki, S. Mitsui and K. T. Mueller, *Mater. Today*, 2013, **16**, 243-248.
5. E. Burger, D. Rebiscoul, F. Bruguier, M. Jublot, J. E. Lartigue and S. Gin, *Appl. Geochem.*, 2013, **31**, 159-170.
6. A. Hoppe, N. S. Gueldal and A. R. Boccaccini, *Biomaterials*, 2011, **32**, 2757-2774.
7. A. Reddy, D. F. Norris, S. S. Momeni, B. Waldo and J. D. Ruby, *J. Am. Dent. Assoc.*, 2016, **147**, 255-263.
8. N. J. Smith and C. G. Pantano, *J. Am. Ceram. Soc.*, 2008, **91**, 736-744.
9. R. G. Iacocca and M. Allgeier, *J. Mater. Sci.*, 2007, **42**, 801-811.
10. V. F. Curto, S. Coyle, R. Byrne, N. Angelov, D. Diamond and F. Benito-Lopez, *Sensor. Actuat. B-Chem.*, 2012, **175**, 263-270.
11. N. Tsomaia, S. L. Brantley, J. P. Hamilton, C. G. Pantano and K. T. Mueller, *Am. Mineral.*, 2003, **88**, 54-67.
12. J. P. Hamilton, S. L. Brantley, C. G. Pantano, L. J. Criscenti and J. D. Kubicki, *Geochim. Cosmochim. Acta*, 2001, **65**, 3683-3702.
13. J. P. Hamilton, C. G. Pantano and S. L. Brantley, *Geochim. Cosmochim. Acta*, 2000, **64**, 2603-2615.
14. J. P. Hamilton and C. G. Pantano, *J. Non-Cryst. Solids*, 1997, **222**, 167-174.
15. J. Declercq, T. Diedrich, M. Perrot, S. R. Gislason and E. H. Oelkers, *Geochim. Cosmochim. Acta*, 2013, **100**, 251-263.
16. D. Wolff-Boenisch, S. R. Gislason, E. H. Oelkers and C. V. Putnis, *Geochim. Cosmochim. Acta*, 2004, **68**, 4843-4858.
17. D. Wolff-Boenisch, S. R. Gislason and E. H. Oelkers, *Geochim. Cosmochim. Acta*, 2004, **68**, 4571-4582.
18. S. R. Gislason and E. H. Oelkers, *Geochim. Cosmochim. Acta*, 2003, **67**, 3817-3832.
19. E. H. Oelkers and S. R. Gislason, *Geochim. Cosmochim. Acta*, 2001, **65**, 3671-3681.
20. G. Berger, C. Claparols, C. Guy and V. Daux, *Geochim. Cosmochim. Acta*, 1994, **58**, 4875-4886.
21. K. G. Knauss, W. L. Bourcier, K. D. McKeegan, C. I. Merzbacher, S. N. Nguyen, F. J. Ryerson, D. K. Smith, H. C. Weed and L. Newton, *MRS Proceedings*, 1989, 371-381.
22. T. Geisler, A. Janssen, D. Scheiter, T. Stephan, J. Berndt and A. Putnis, *J. Non-Cryst. Solids*, 2010, **356**, 1458-1465.
23. R. H. Doremus, *J. Non-Cryst. Solids*, 1975, **19**, 137-144.
24. B. C. Bunker, *J. Non-Cryst. Solids*, 1994, **179**, 300-308.
25. J. Hopf, J. R. Eskelsen, M. Chiu, A. Ievlev, O. S. Ovchinnikova, D. Leonard and E. M. Pierce, *Geochim. Cosmochim. Acta*, 2018, **229**, 65-84.
26. J. D. Vienna, J. V. Ryan, S. Gin and Y. Inagaki, *Int. J. Appl. Glass Sci.*, 2013, **4**, 283-294.
27. C. Lenting, O. Plümper, M. Kilburn, P. Guagliardo, M. Klinkenberg and T. Geisler, *npj Materials Degradation*, 2018, **2**, 28.
28. S. Gin, L. Neill, M. Fournier, P. Frugier, T. Ducasse, M. Tribet, A. Abdelouas, B. Parruzot, J. Neeway and N. Wall, *Chem. Geol.*, 2016, **440**, 115-123.
29. Q. Zheng, R. E. Youngman, C. L. Hogue, J. C. Mauro, M. Potuzak, M. M. Smedskjær and Y. Yue, *Phys. Rev. B*, 2012, **86**, 054203.
30. T. Geisler, T. Nagel, M. R. Kilburn, A. Janssen, J. P. Icenhower, R. O. Fonseca, M. Grange and A. A. Nemchin, *Geochim. Cosmochim. Acta*, 2015, **158**, 112-129.
31. Y. Wang, C. F. Jove-Colon and K. L. Kuhlman, *Sci. Rep.*, 2016, **6**, 30256.

32. E. M. Pierce, L. R. Reed, W. J. Shaw, B. P. McGrail, J. P. Icenhower, C. F. Windisch, E. A. Cordova and J. Broady, *Geochim. Cosmochim. Acta*, 2010, **74**, 2634-2654.
33. R. Balzer, H. Behrens, S. Schuth, T. Waurischk, S. Reinsch, R. Müller, M. Fechtelkord and J. Deubener, *J. Non-Cryst. Solids*, 2019, **519**, 119454.
34. D. Massiot, F. Fayon, M. Capron, I. King, S. Le Calvé, B. Alonso, J. O. Durand, B. Bujoli, Z. Gan and G. Hoatson, *Magn. Reson. Chem.*, 2002, **40**, 70-76.
35. D. Massiot, C. Bessada, J. Coutures and F. Taulelle, *J. Magn. Reson.*, 1990, **90**, 231-242.
36. ASTM (American Society for Testing and Materials) Standard: C 1220-10, *ASTM International*, West Conshohocken, PA, 1999.
37. J. H. Scofield, *Theoretical photoionization cross sections from 1 to 1500 keV*, California Univ., Livermore. Lawrence Livermore Lab., 1973.
38. G. C. Smith, *J. Electron. Spectrosc.*, 2005, **148**, 21-28.
39. A. Zeidler, K. Wezka, D. A. J. Whittaker, P. S. Salmon, A. Baroni, S. Klotz, H. E. Fischer, M. C. Wilding, C. L. Bull, M. G. Tucker, M. Salanne, G. Ferlat and M. Micoulaut, *Phys. Rev. B*, 2014, **90**.
40. L.-S. Du and J. F. Stebbins, *J. Non-Cryst. Solids*, 2005, **351**, 3508-3520.
41. M. M. Smedskjaer, Q. Zheng, J. C. Mauro, M. Potuzak, S. Mørup and Y. Yue, *J. Non-Cryst. Solids*, 2011, **357**, 3744-3750.
42. L. Züchner, J. C. C. Chan, W. Müller-Warmuth and H. Eckert, *J. Phys. Chem. B*, 1998, **102**, 4495-4506.
43. S. Kapoor, R. E. Youngman, K. Zakharchuk, A. Yaremchenko, N. J. Smith and A. Goel, *J. Phys. Chem. B*, 2018, **122**, 10913-10927.
44. M. Bertmer, L. Züchner, J. C. Chan and H. Eckert, *J. Phys. Chem. B*, 2000, **104**, 6541-6553.
45. H. R. Fernandes, S. Kapoor, Y. Patel, K. Ngai, K. Levin, Y. Germanov, L. Krishtopa, S. Kroeker and A. Goel, *J. Non-Cryst. Solids*, 2018, **502**, 142-151.
46. E. I. Morin and J. F. Stebbins, *J. Non-Cryst. Solids*, 2016, **432**, 384-392.
47. E. I. Morin, J. Wu and J. F. Stebbins, *Appl. Phys. A*, 2014, **116**, 479-490.
48. S. K. Lee and J. F. Stebbins, *Am. Mineral.*, 1999, **84**, 937-945.
49. S. Sen and R. E. Youngman, *J. Phys. Chem. B*, 2004, **108**, 7557-7564.
50. M. J. Toplis, S. C. Kohn, M. E. Smith and I. J. F. Poplett, *Am. Mineral.*, 2000, **85**, 1556-1560.
51. D. R. Neuville, L. Cormier and D. Massiot, *Chem. Geol.*, 2006, **229**, 173-185.
52. K. Januchta, R. E. Youngman, A. Goel, M. Bauchy, S. J. Rzoska, M. Bockowski and M. M. Smedskjaer, *J. Non-Cryst. Solids*, 2017, **460**, 54-65.
53. L. M. Thompson and J. F. Stebbins, *J. Non-Cryst. Solids*, 2012, **358**, 1783-1789.
54. D. R. Neuville, presented in part at the ICG Annual Meeting 2018, Yokohama, Japan, 2018.
55. J. Wu and J. F. Stebbins, *J. Non-Cryst. Solids*, 2009, **355**, 556-562.
56. M. M. Smedskjaer, J. C. Mauro, R. E. Youngman, C. L. Hogue, M. Potuzak and Y. Yue, *J. Phys. Chem. B*, 2011, **115**, 12930-12946.
57. M. M. Smedskjaer, R. E. Youngman, S. Striepe, M. Potuzak, U. Bauer, J. Deubener, H. Behrens, J. C. Mauro and Y. Yue, *Sci. Rep.*, 2014, **4**, 3770.
58. D. J. Wesolowski and D. A. Palmer, *Geochim. Cosmochim. Acta*, 1994, **58**, 2947-2969.
59. A. Paul, *J. Mater. Sci.*, 1977, **12**, 2246-2268.
60. W. L. Ebert, *Comparison of the results of short-term static tests and single-pass flow-through tests with LRM glass (ANL-06/51)*, Argonne National Laboratory (ANL), 2007.
61. S. Gin, P. Frugier, P. Jollivet, F. Bruguier and E. Curti, *Int. J. Appl. Glass Sci.*, 2013, **4**, 371-382.
62. M. Fournier, A. Ull, E. Nicoleau, Y. Inagaki, M. Odorico, P. Frugier and S. Gin, *J. Nucl. Mater.*
63. W. L. Ebert and J. K. Bates, *Nucl. Tech.*, 1993, **104**, 372-384.
64. W. L. Ebert, *The effects of the glass surface area/solution volume ratio on glass corrosion: a critical review*, Argonne National Laboratory, 1995.
65. J. Kragten, *Analyst*, 1994, **119**, 2161-2165.

66. L. J. Criscenti, S. L. Brantley, K. T. Mueller, N. Tsomaia and J. D. Kubicki, *Geochim. Cosmochim. Acta*, 2005, **69**, 2205-2220.
67. W. H. Casey, H. R. Westrich and G. R. Holdren, *Am. Mineral.*, 1991, **76**, 211-217.
68. E. H. Oelkers and J. Schott, *Geochim. Cosmochim. Acta*, 1995, **59**, 5039-5053.
69. F. Devreux, P. Barboux, M. Filoche and B. Sapoval, *J. Mater. Sci.*, 2001, **36**, 1331-1341.
70. B. C. Bunker, G. W. Arnold, D. E. Day and P. Bray, *J. Non-Cryst. Solids*, 1986, **87**, 226-253.
71. J. T. Kloprogge, L. V. Duong, B. J. Wood and R. L. Frost, *J. Colloid. Interf. Sci.*, 2006, **296**, 572-576.
72. E. Paparazzo, *Surf. Interface Analysis*, 1988, **12**, 115-118.
73. M. Remy, M. Genet, P. Notté, P. Lardinois and G. Poncelet, *Microporous Mater.*, 1993, **2**, 7-15.
74. T. Ebina, T. Iwasaki, A. Chatterjee, M. Katagiri and G. D. Stucky, *J. Phys. Chem. B*, 1997, **101**, 1125-1129.
75. G. W. Tasker, D. R. Uhlmann, P. I. K. Onorato, M. N. Alexander and C. W. Struck, *J. Phys. Colloq.*, 1985, **46**, C8-273.
76. J. Banerjee, S. H. Kim and C. G. Pantano, *J. Non-Cryst. Solids*, 2016, **450**, 185-193.
77. S. K. Lee and J. F. Stebbins, *J. Phys. Chem. B*, 2000, **104**, 4091-4100.
78. W. Loewenstein, *Am. Mineral.*, 1954, **39**, 92-96.
79. L.-S. Du and J. F. Stebbins, *Solid State Nucl. Mag.*, 2005, **27**, 37-49.
80. S. K. Lee, C. B. Musgrave, P. Zhao and J. F. Stebbins, *J. Phys. Chem. B*, 2001, **105**, 12583-12595.

Tables

Table 1. Experimental compositions (within ±0.5 mol. %), density (ρ), molar volume (V_M), and T_g of the studied glass series.

Sample ID	Experimental (mol. %)				ρ (±0.3 %) (g/cm^3)	V_M (±0.3 %) (cm^3/mol)	T_g (°C)
	Na_2O	Al_2O_3	B_2O_3	SiO_2			
B-0	25.1	25.9	--	49.0	2.458	29.05	839±2
B-5	25.2	25.4	5.1	44.3	2.433	29.46	719±5
B-10	24.8	26.0	9.1	40.0	2.415	29.94	679±11
B-15	24.6	26.6	14.0	34.8	2.391	30.54	635±4
B-20	25.0	26.1	19.2	29.7	2.369	30.95	591±2
B-25	25.1	26.0	24.3	24.6	2.339	31.54	549±3
B-30	24.8	26.0	28.6	20.5	2.318	32.00	532±1
B-35	24.8	25.7	33.8	15.7	2.296	32.47	513±1
B-40	25.0	25.6	38.7	10.7	2.261	33.15	502±1
B-45	24.8	25.3	44.7	5.2	2.246	33.58	491±1
B-50	25.2	25.5	49.3	--	2.227	34.11	486±1

Table 2. B and Al % structural speciation in the glassy network (within ±0.5 %), as extracted from ^{11}B and ^{27}Al MAS NMR. Calculated NBO fractions as derived from Al and B speciation are also shown.

Sample ID	^{11}B MAS NMR		^{27}Al MAS NMR		% NBO in Network (Calculated)*
	N_3	N_4	AlO_4	AlO_5	
B-0	--	--	98.7	1.3	-0.5
B-5	99.6	0.4	98.8	1.2	0.1
B-10	99.5	0.5	98.3	1.7	-0.8
B-15	99.4	0.6	98.0	2.0	-1.5
B-20	98.9	1.1	98.7	1.3	-0.9
B-25	98.0	2.0	98.5	1.5	-1.0
B-30	97.6	2.4	98.6	1.4	-1.3
B-35	96.5	3.5	97.5	2.5	-1.2
B-40	95.3	4.7	97.3	2.7	-1.5
B-45	94.6	5.4	95.6	4.4	-1.5
B-50	94.0	6.0	94.1	5.9	-1.4

*Note: Negative NBO values displayed occur as a result of lower Na_2O content in the glass than that necessary to charge compensate AlO_4 and/or BO_4 units

Table 3. Normalized loss rates of Na, Al, B, and Si for the studied glass in pH = 2 solutions. These rates were determined by linearly fitting normalized loss vs. time plots. Rates have been compared according to experimental B/(Al+Si) ratios in the glass.

		Normalized Loss Rates (g-glass/[m^{2}h])							
Sample ID	**B/(Si+Al) Ratio**	**Na**	**Na-error**	**Al**	**Al-error**	**B**	**B-error**	**Si**	**Si-error**
B-0	0.00	3.2	±0.3	2.9	±0.3	--	--	3.3	±0.3
B-5	0.11	4.2	±0.1	4.1	±0.1	2.8	±0.2	3.2	±1.7
B-10	0.20	6.5	±0.3	6.3	±0.2	4.4	±0.2	7.0	±0.2
B-15	0.32	5.8	±0.3	5.4	±0.07	3.93	±0.06	6.0	±0.1
B-20	0.47	7.1	±0.5	6.6	±0.5	4.9	±0.4	6.8	±0.6
B-25	0.63	8.9	±1.8	8.1	±1.7	6.2	±1.3	8.0	±1.5
B-30	0.79	8.3	±0.2	7.7	±0.2	6.1	±0.2	8.45	±0.07
B-35	1.00	9.6	±0.2	8.9	±0.3	7.0	±0.2	8.8	±0.7
B-40	1.25	12.3	±2.2	11.2	±2.1	8.9	±1.8	9.9	±2.8
B-45	1.59	16.4	±0.9	13.7	±0.9	11.6	±0.7	*	*
B-50	1.93	18.2	±0.1	14.1	±0.1	13.26	±0.07	--	--

*Dissolution rate was not able to be extracted due to non-linear behavior in the forward rate regime and/or concentrations near the ICP-OES detection limits

Table 4. Surface compositions of B-5, B-25, and B-45 samples as measured in the top ~5-10 nm via XPS analysis (atomic percentages accurate within ±5 %). In each sample, we have compared compositions of polished and corroded samples to the bulk compositions measured using ICP-OES.

Element (at. % by XPS)	**Sample**								
	B-5			**B-25**			**B-45**		
	Bulk	**Polished Surface**	**Corroded Surface**	**Bulk**	**Polished Surface**	**Corroded Surface**	**Bulk**	**Polished Surface**	**Corroded Surface**
Na	14.0	12.2	12.6	12.5	10.2	9.1	11.3	10.0	0.9
Al	14.1	13.0	13.2	13.0	11.7	13.6	11.5	10.9	26.3
B	2.8	7.0	3.8	12.1	13.7	9.7	20.3	22.6	4.1
Si	12.3	12.6	11.6	6.1	7.2	6.3	1.2	1.6	2.9
O	56.9	55.3	58.8	56.2	57.2	61.2	55.7	55.0	65.8

Table 5. Surface compositions of B-5, B-25, and B-45 samples as measured in the top 100-300 nm via RBS analysis (atomic percentages accurate within ±4 %). In each sample, we have compared compositions of polished and corroded samples to the bulk compositions measured using ICP-OES

Element (at. % by RBS)	**Sample**								
	B-5			**B-25**			**B-45**		
	Bulk	**Polished Surface**	**Corroded Surface**	**Bulk**	**Polished Surface**	**Corroded Surface**	**Bulk**	**Polished Surface**	**Corroded Surface**
Na	14.0	13.9	13.0	12.5	12.1	11.8	11.3	11.3	4.8
Al	14.1	13.6	13.8	13.0	9.8	12.3	11.5	11.0	18.3
B*	2.8	2.8	3.0	12.1	15.8	12.6	20.3	21.8	18.8
Si	12.3	11.8	11.8	6.1	7.8	6.3	1.2	1.1	1.1
O	56.9	57.8	58.4	56.2	54.4	56.9	55.7	54.7	57.0

*Note: B concentration estimated by difference

Figure Captions

Figure 1. (a) ^{11}B MAS NMR and (b) ^{27}Al MAS NMR spectral overlays of studied glasses. Trends according to increasing *x* (B_2O_3 content) can be seen in each plot. The (*) symbol in ^{27}Al spectra represents a background signal from the rotor.

Figure 2. (a) T_g and average Al and B coordination in the studied glasses as a function of B/(Al+Si) molar ratio. T_g is displayed on the left axis and both B and Al coordination are shown on the right axes. The fit of T_g displayed was performed using an exponential function to exhibit its non-linear behavior with composition. (b) Fractional display of network-forming species contained in the studied glass series according to B/(Al+Si) ratio, which have been normalized to 100 %.

Figure 3. Plots of normalized loss (g/m^2) of each element present in the glass as a function of time (hours) for (a) B-0, (b) B-5, (c) B-25, (d) B-45, and (e) B-50.

Figure 4. Solution pH as a function of glass B_2O_3 content (mol. %) in pH = 2 starting solution. The data points highlighted in blue represent pH after 12 h dissolution experiments while points displayed in gray represent the pH data spread along the course of corrosion experiments for each glass composition.

Figure 5. Na, Al, B, and Si normalized loss rates in acidic solutions as a function of B/(Al+Si) molar ratio.

Figure 6. (a) ^{27}Al MAS NMR spectra of B-0, B-25, and B-50 grains recovered from dissolution experiments, as compared with the pre-corroded glass spectra. (b) ^{11}B MAS NMR spectra of B-25 and B-50 grains recovered from dissolution experiments.

Figure 7. (a) Al 2p, (b) Na 1s, (c) B 1s, (d) Si 2p, and (e) Al 2p XPS spectra of polished and corroded B-45 glass coupons (12 hours at pH = 2).

Figure 8. (a) RBS and (b) ERDA spectra of polished and corroded B-45 glass coupons (12 hours at pH = 2).

Figures

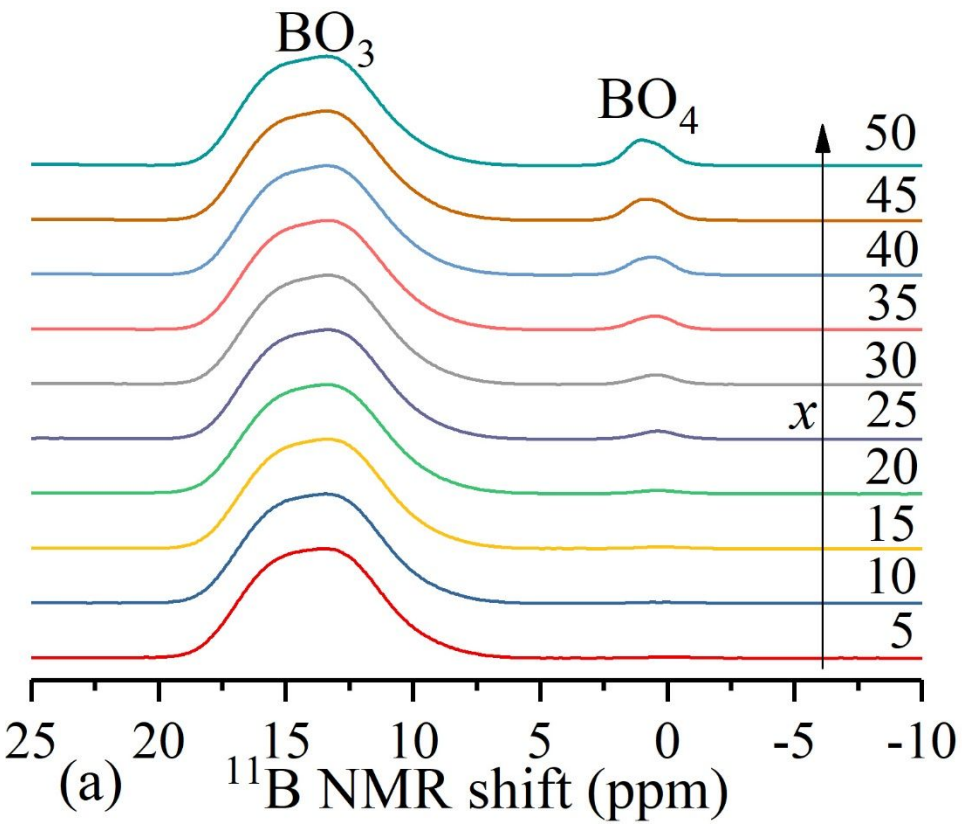
BO3
BO4
50
45
40
35
30
x
25
20
15
10
5
25
20
15
10
5
0
-5
-10
(a)
11B NMR shift (ppm)

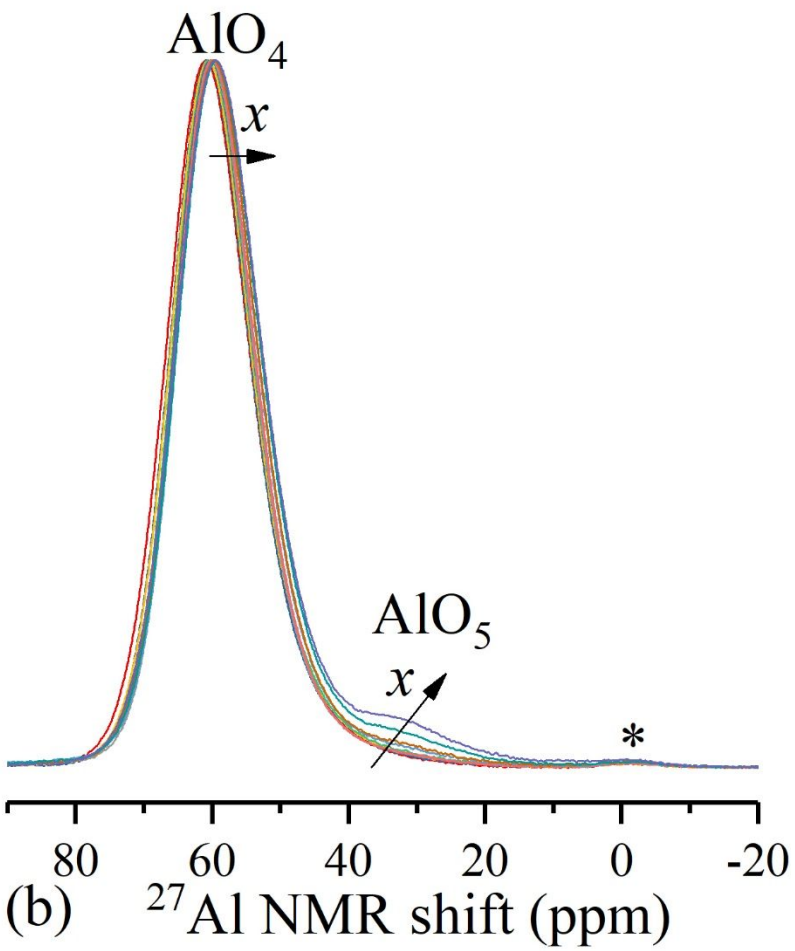

Figure 1. (a) ^{11}B MAS NMR and (b) ^{27}Al MAS NMR spectral overlays of studied glasses. Trends according to increasing x (B_2O_3 content) can be seen in each plot. The (*) symbol in ^{27}Al spectra represents a background signal from the rotor.

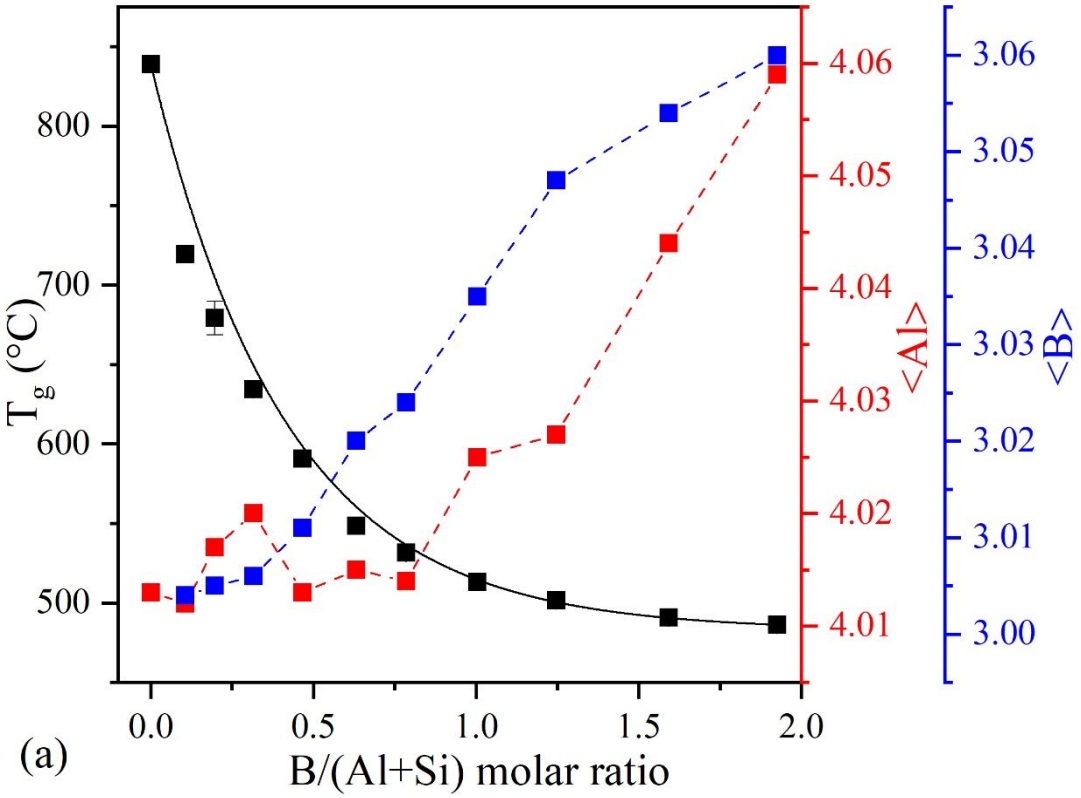
800
700
600
500
T_g (°C)
4.06
4.05
4.04
4.03
4.02
4.01
<Al>
3.06
3.05
3.04
3.03
3.02
3.01
3.00
<B>
0.0
0.5
1.0
1.5
2.0
B/(Al+Si) molar ratio
(a)

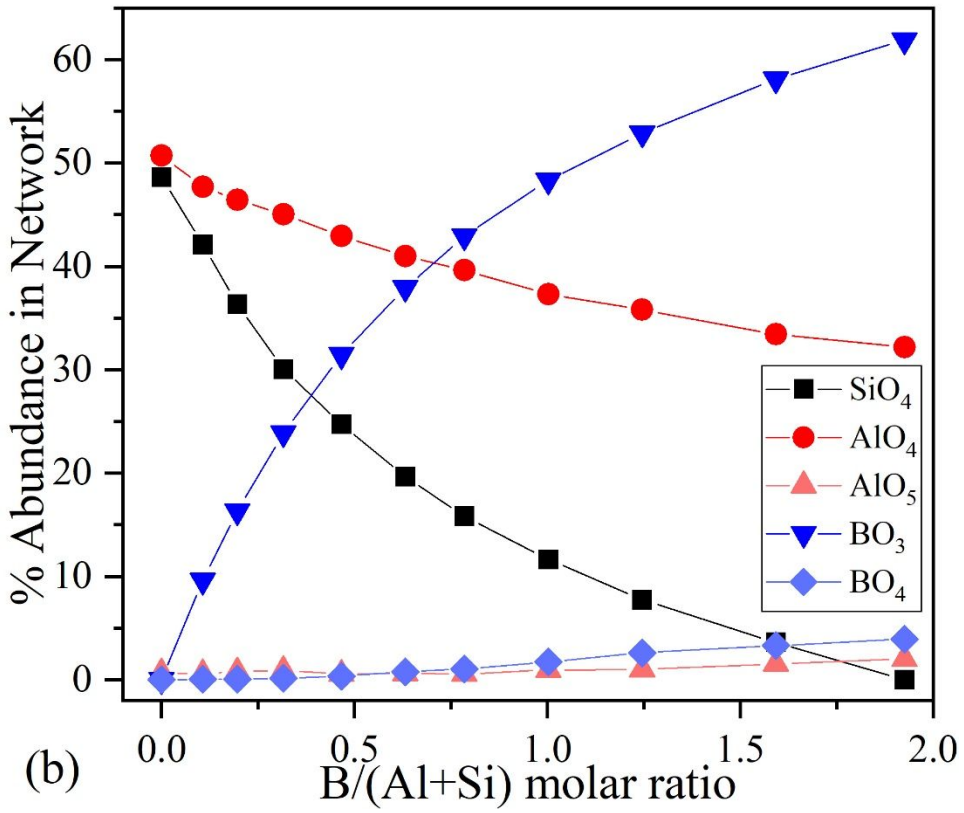
% Abundance in Network
60
50
40
30
20
10
0
SiO_4
AlO_4
AlO_5
BO_3
BO_4
0.0
0.5
1.0
1.5
2.0
B/(Al+Si) molar ratio
(b)

Figure 2. (a) T_g and average Al and B coordination in the studied glasses as a function of B/(Al+Si) molar ratio. T_g is displayed on the left axis and both B and Al coordination are shown on the right axes. The fit of T_g displayed was performed using an exponential function to exhibit its non-linear behavior with composition. (b) Fractional display of network-forming species contained in the studied glass series according to B/(Al+Si) ratio, which have been normalized to 100 %.

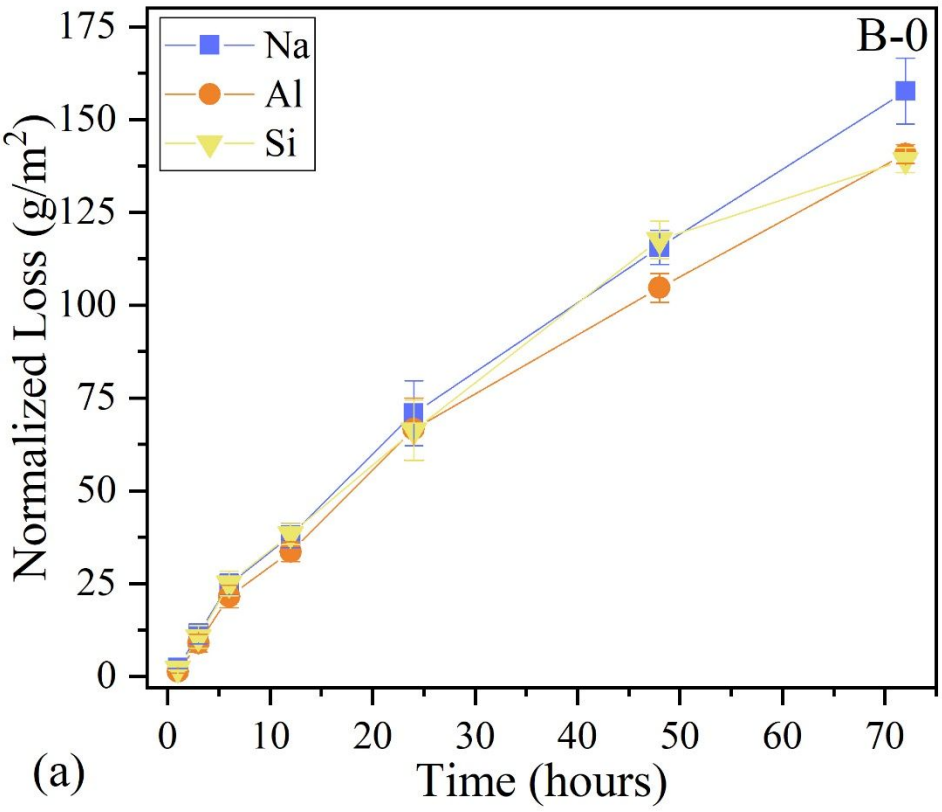

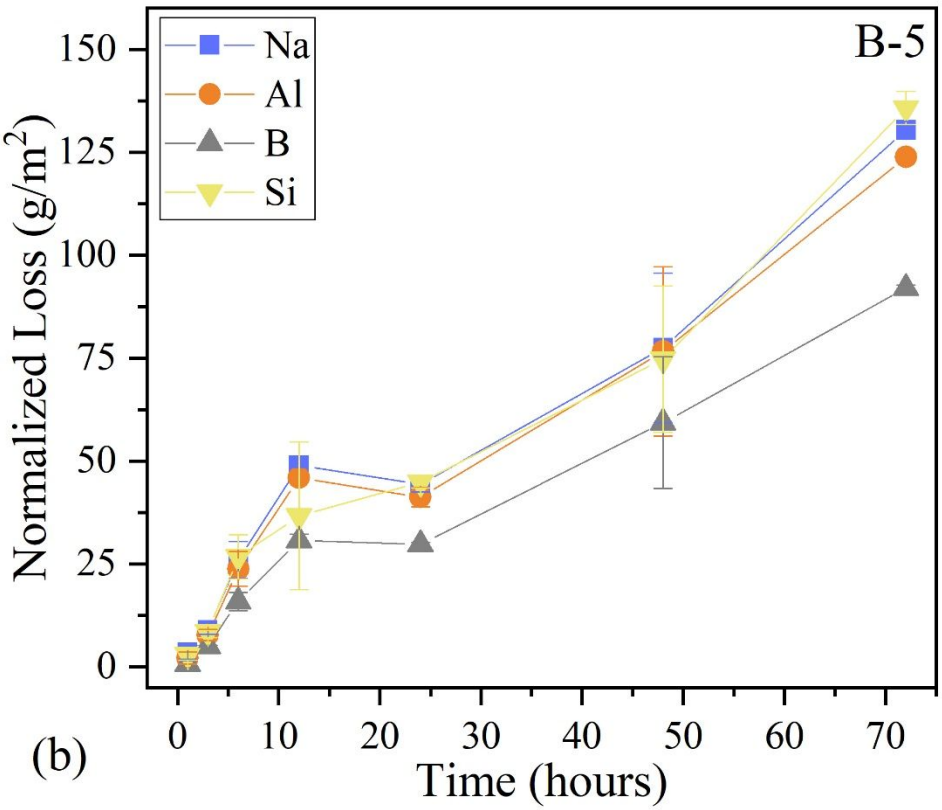
B-5
Na
Al
B
Si
Normalized Loss (g/m^2)
Time (hours)
0
25
50
75
100
125
150
0
10
20
30
40
50
60
70

(b)

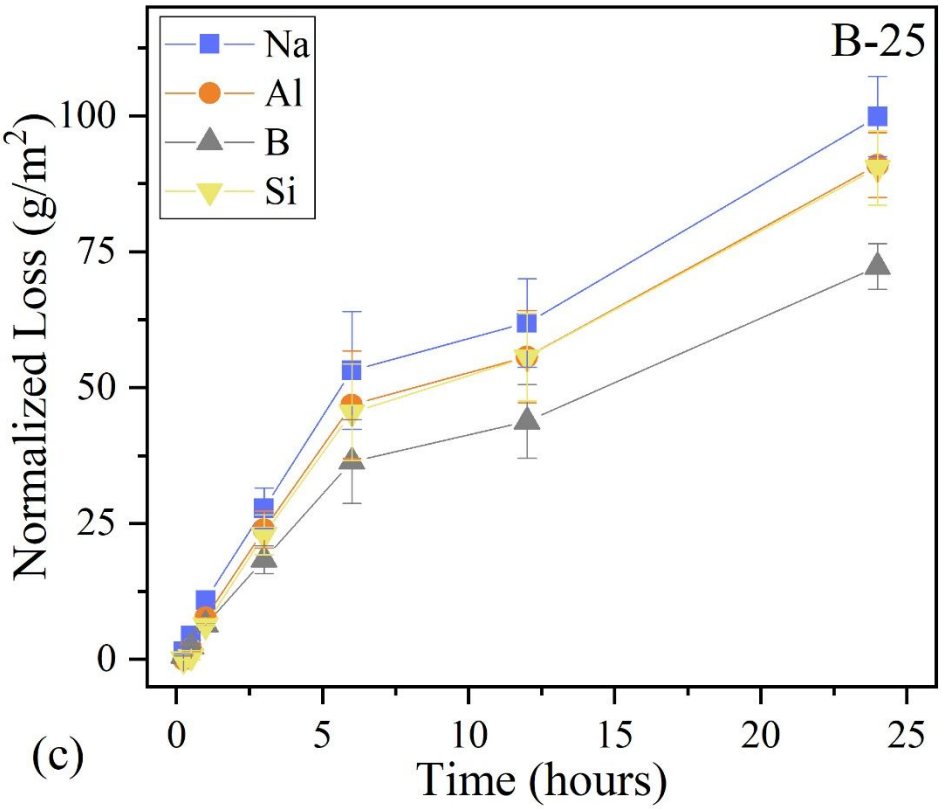
B-25
Na
Al
B
Si
Normalized Loss (g/m^2)
Time (hours)
0
25
50
75
100
0
5
10
15
20
25

(c)

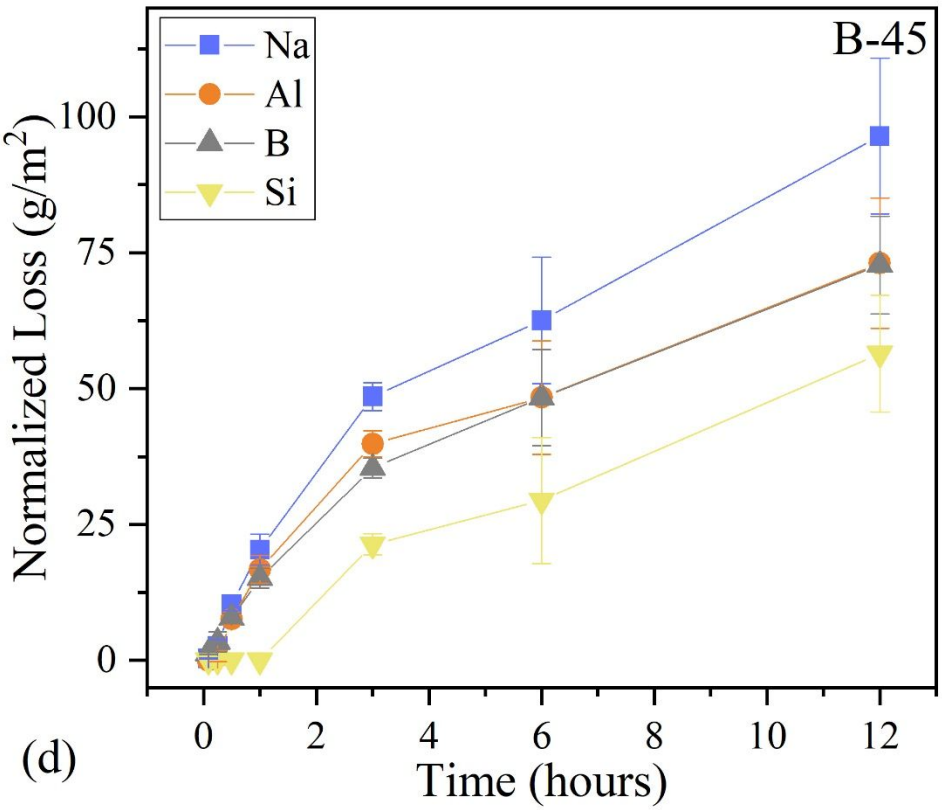
B-45
Na
Al
B
Si
Normalized Loss (g/m^2)
0
25
50
75
100
0
2
4
6
8
10
12
Time (hours)
(d)

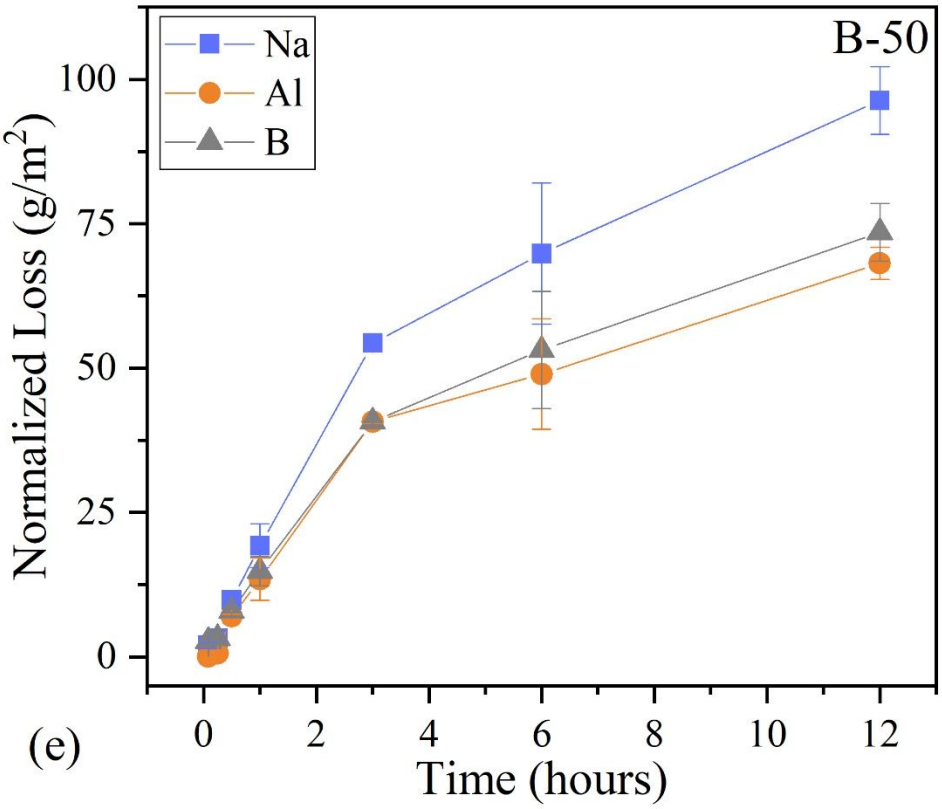
B-50
Na
Al
B
Normalized Loss (g/m^2)
0
25
50
75
100
0
2
4
6
8
10
12
Time (hours)
(e)

Figure 3. Plots of normalized loss (g/m^2) of each element present in the glass as a function of time (hours) for (a) B-0, (b) B-5, (c) B-25, (d) B-45, and (e) B-50.

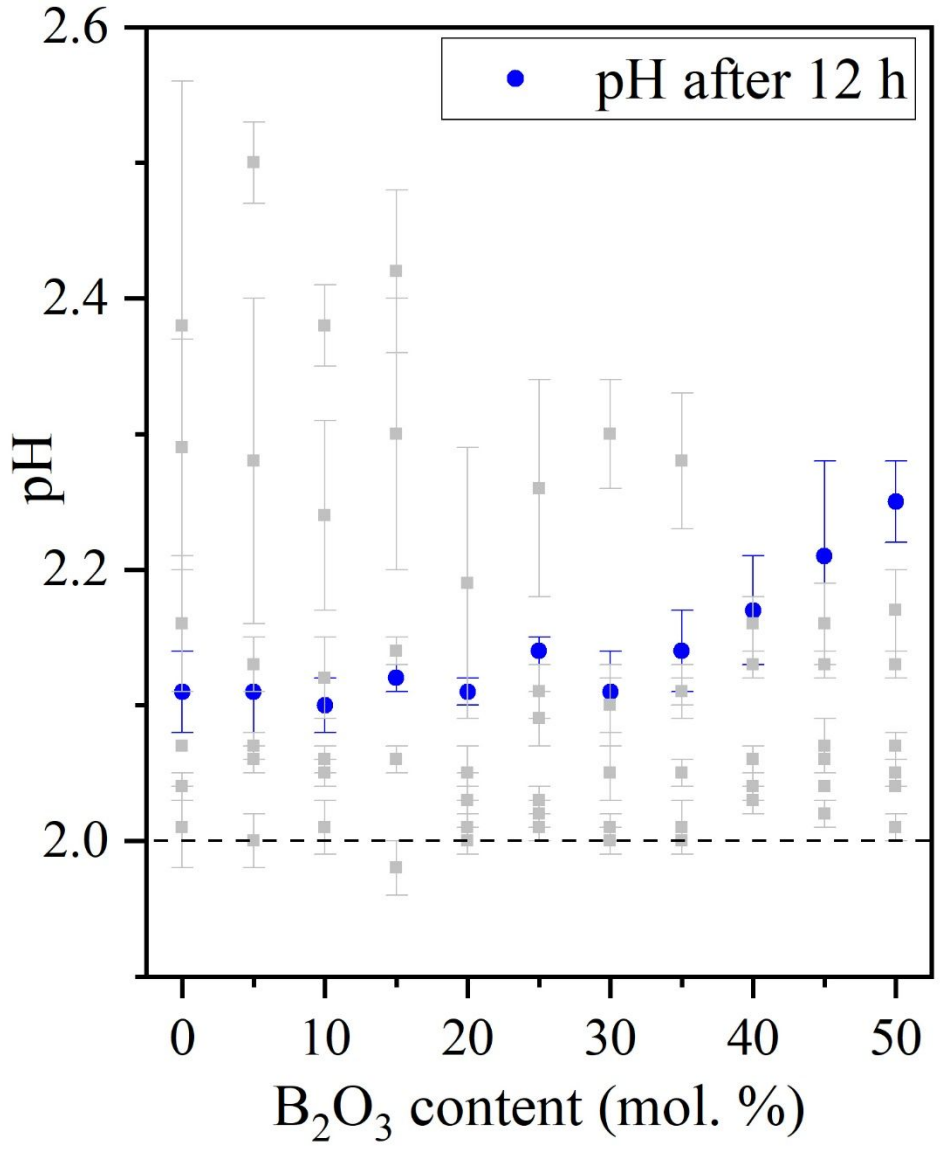

Figure 4. Solution pH as a function of glass B_2O_3 content (mol. %) in pH = 2 starting solution. The data points highlighted in blue represent pH after 12 h dissolution experiments while points displayed in gray represent the pH data spread along the course of corrosion experiments for each glass composition.

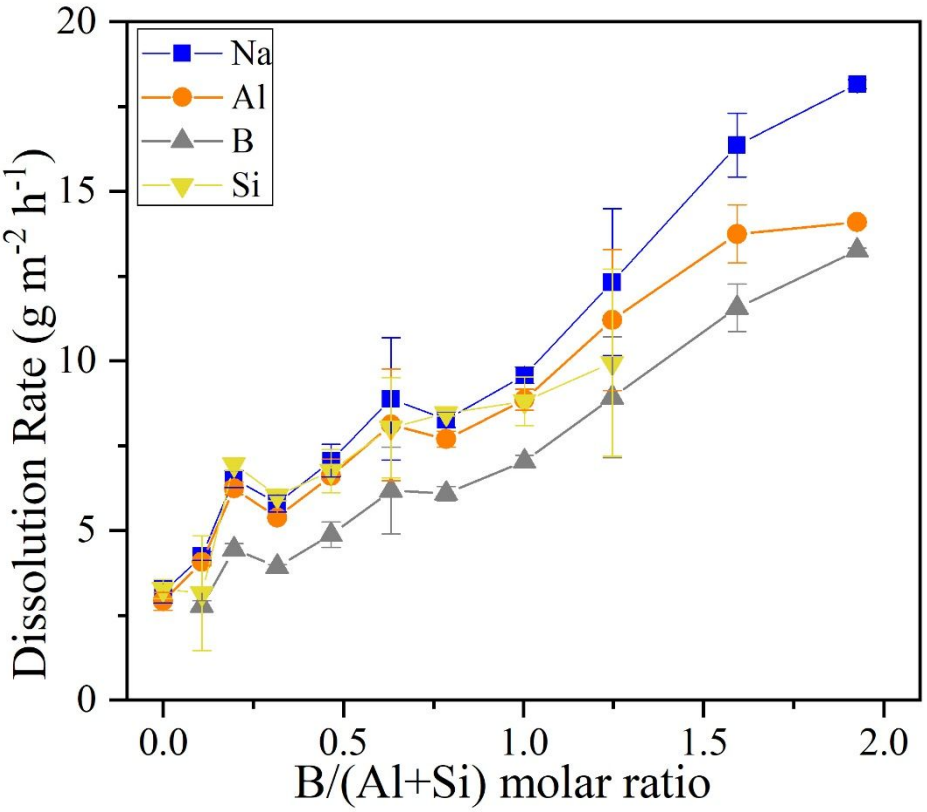

Figure 5. Na, Al, B, and Si normalized loss rates in acidic solutions as a function of B/(Al+Si) molar ratio.

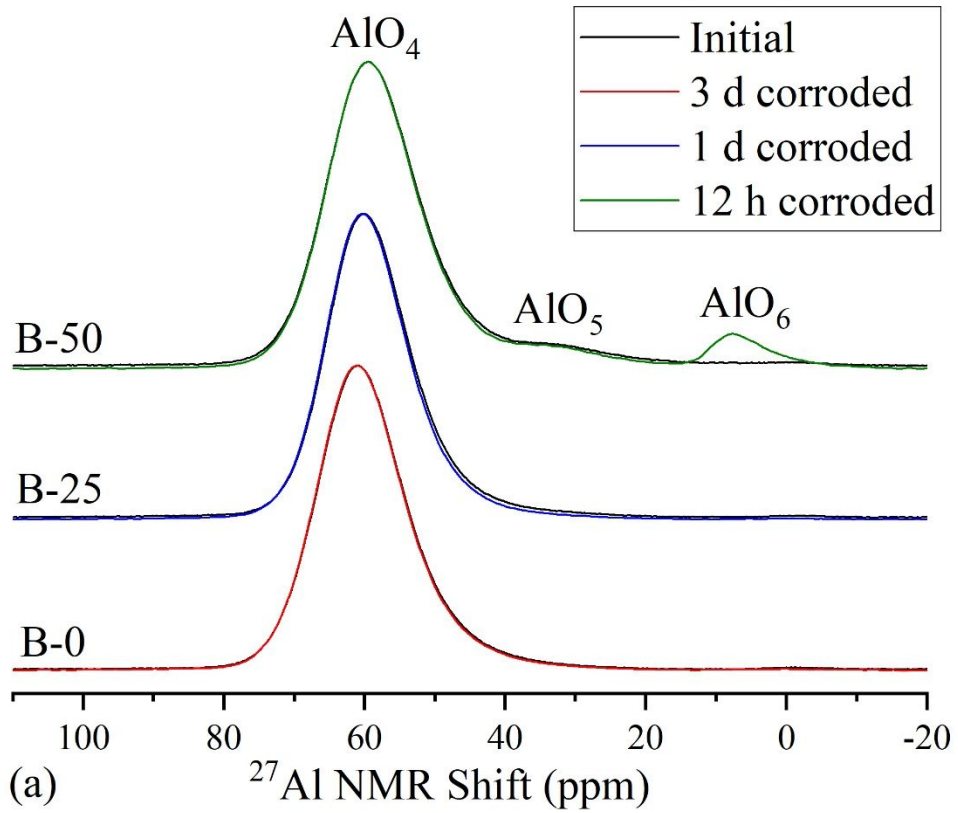
AlO4
Initial
3 d corroded
1 d corroded
12 h corroded
AlO5
AlO6
B-50
B-25
B-0
100
80
60
40
20
0
-20
(a)
27Al NMR Shift (ppm)

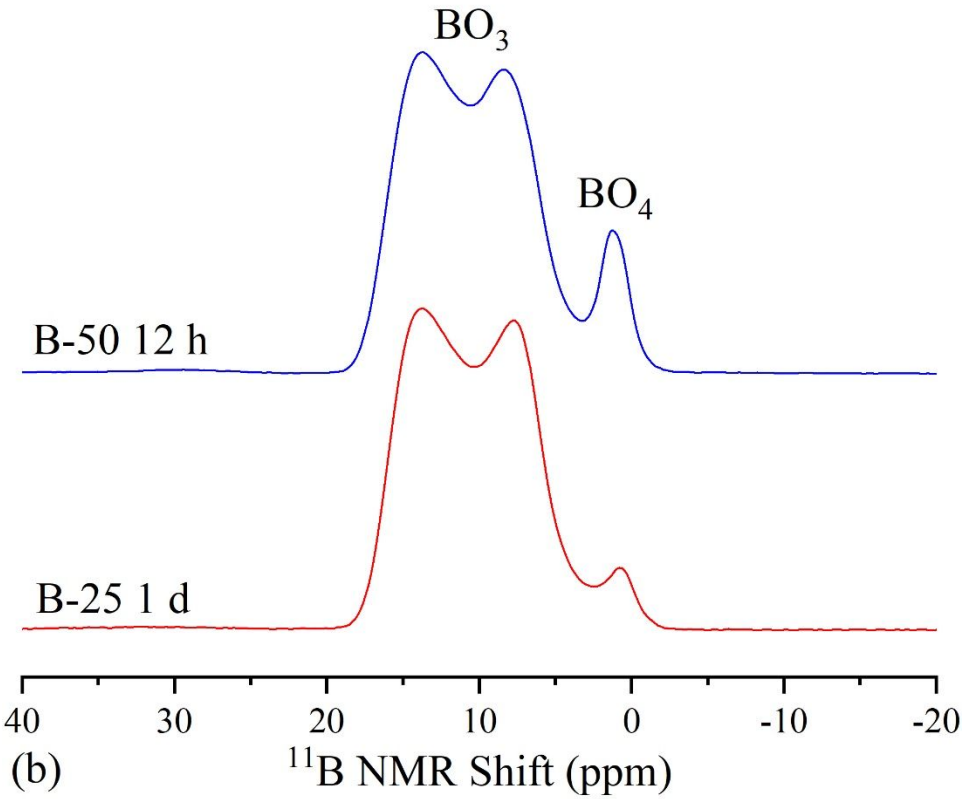
BO3
BO4
B-50 12 h
B-25 1 d
40
30
20
10
0
-10
-20
(b)
11B NMR Shift (ppm)

Figure 6. (a) ^{27}Al MAS NMR spectra of B-0, B-25, and B-50 grains recovered from dissolution experiments, as compared with the pre-corroded glass spectra. (b) ^{11}B MAS NMR spectra of B-25 and B-50 grains recovered from dissolution experiments.

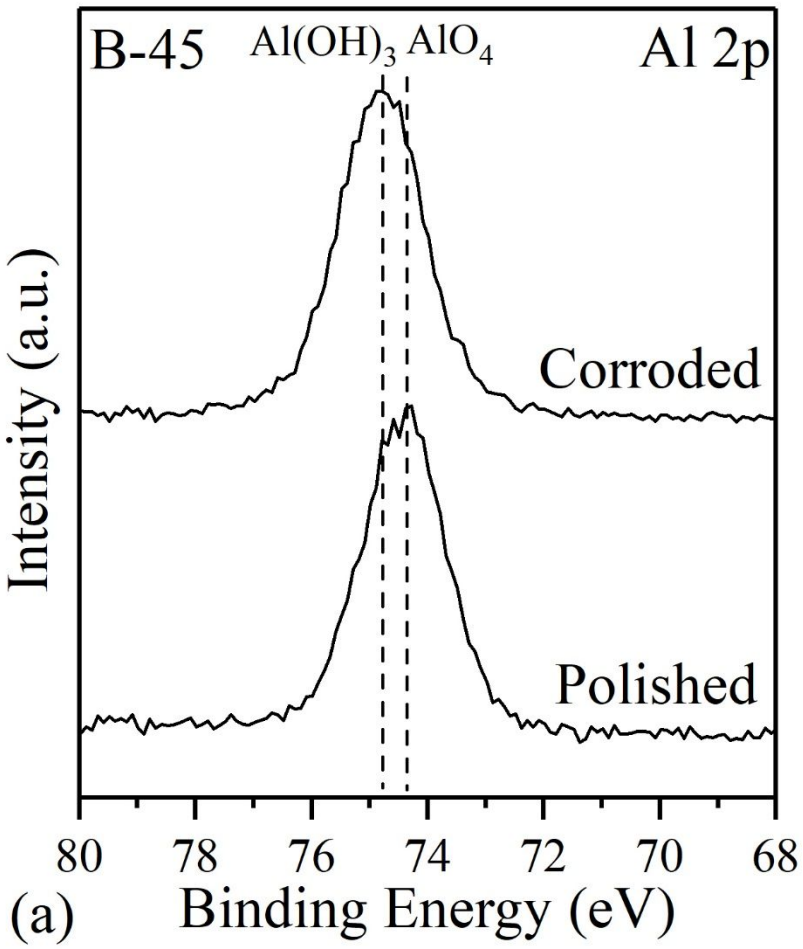

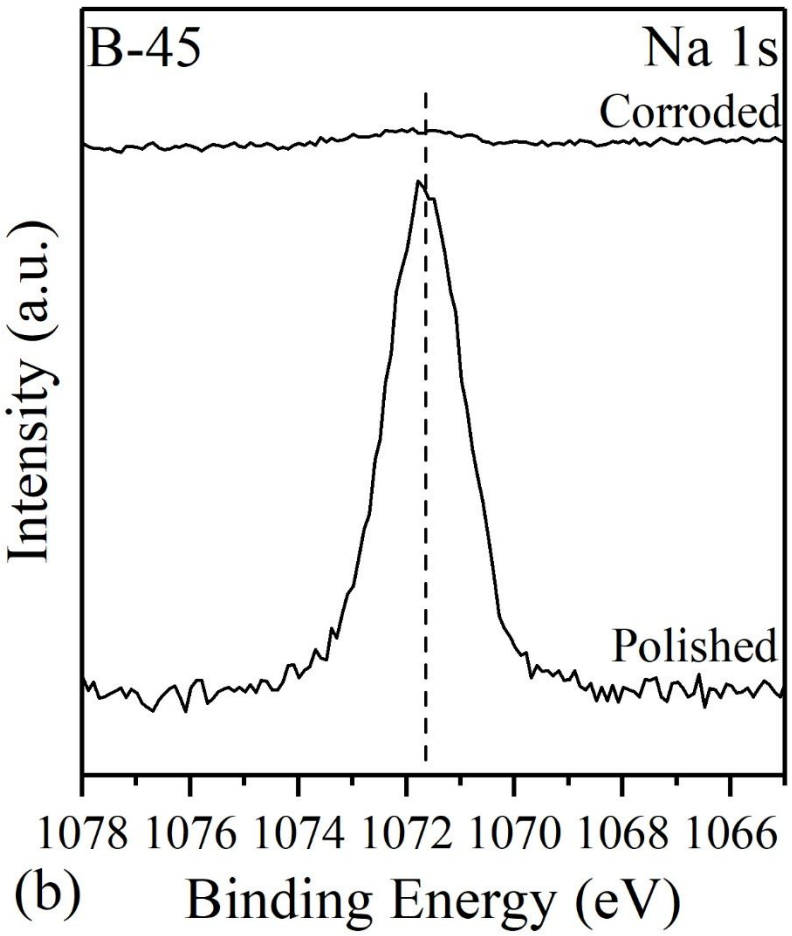
B-45
Na 1s
Corroded
Polished
Intensity (a.u.)
1078 1076 1074 1072 1070 1068 1066
(b) Binding Energy (eV)

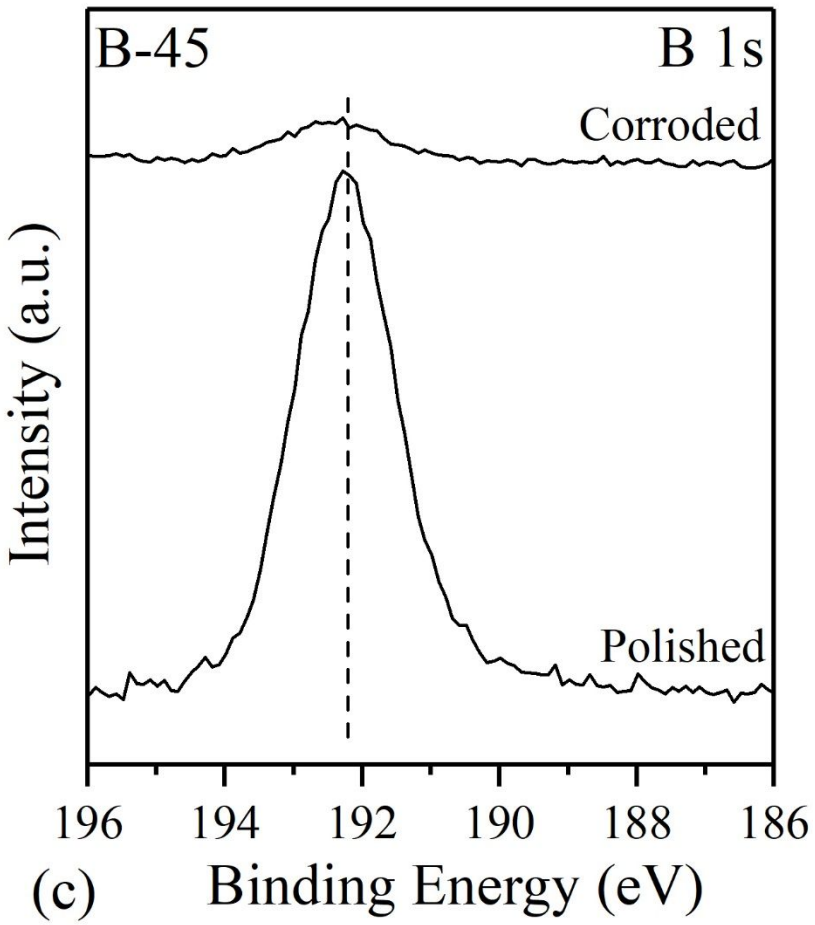
B-45
B 1s
Corroded
Polished
Intensity (a.u.)
196
194
192
190
188
186
Binding Energy (eV)

(c)

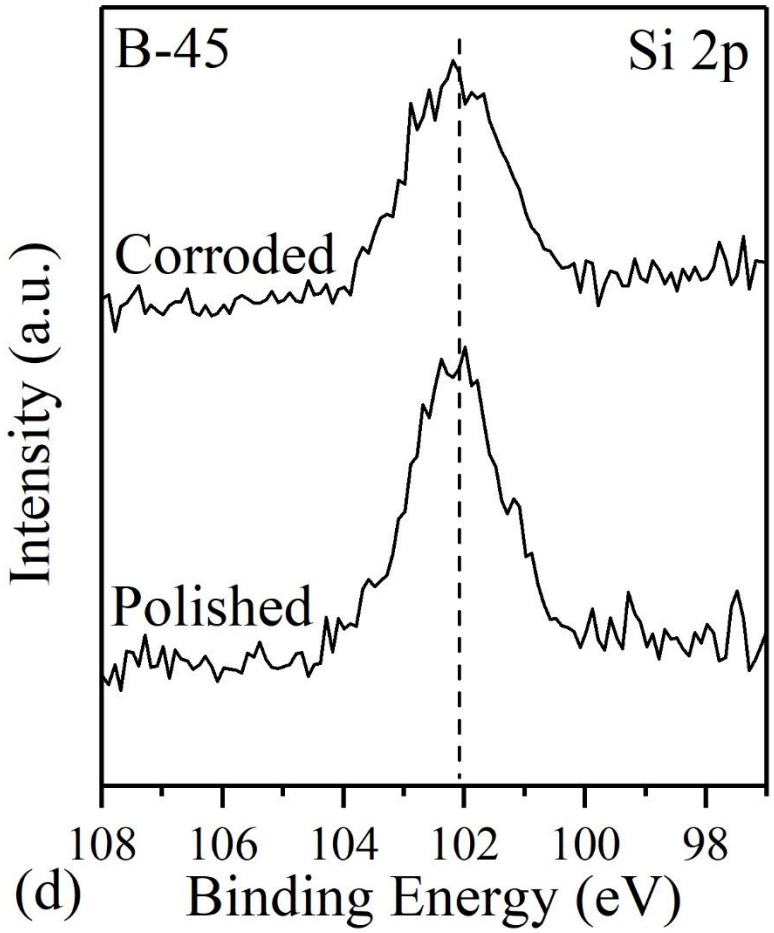
B-45
Si 2p
Corroded
Polished
Intensity (a.u.)
108
106
104
102
100
98
Binding Energy (eV)

(d)

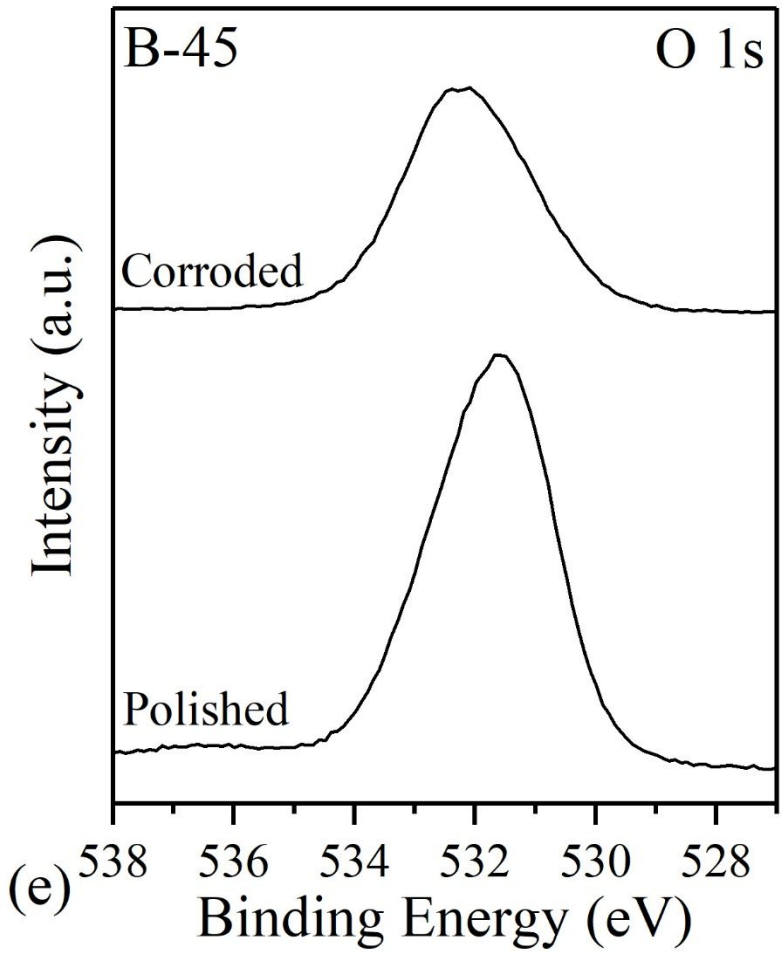

Figure 7. (a) Al 2p, (b) Na 1s, (c) B 1s, (d) Si 2p, and (e) Al 2p XPS spectra of polished and corroded B-45 glass coupons (12 hours at pH = 2).

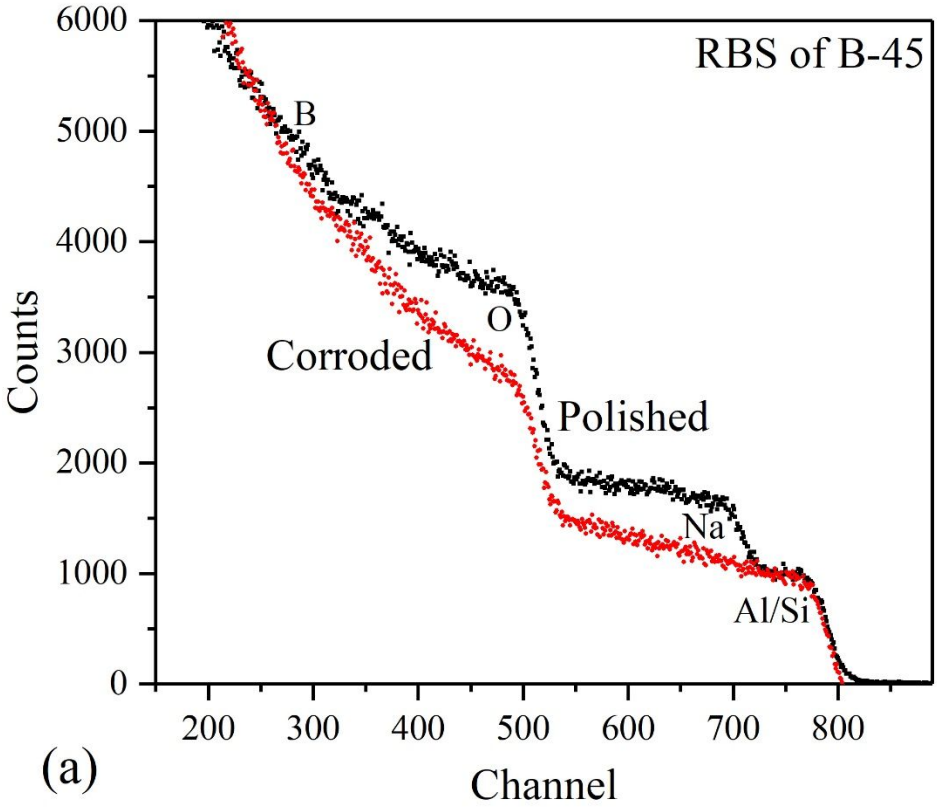
RBS of B-45
B
O
Corroded
Polished
Na
Al/Si
Counts
Channel
6000
5000
4000
3000
2000
1000
0
200
300
400
500
600
700
800
(a)

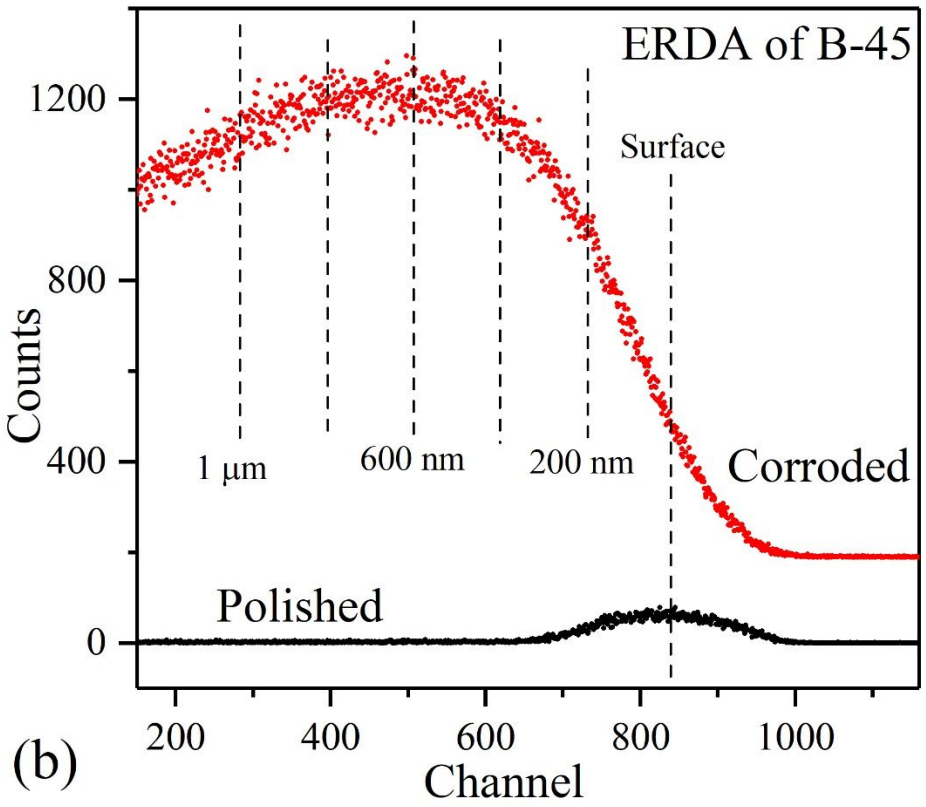

Figure 8. (a) RBS and (b) ERDA spectra of polished and corroded B-45 glass coupons (12 hours at pH = 2).